

Photoresponse of ^{60}Ni below 10-MeV excitation energy: Evolution of dipole resonances in $f p$ -shell nuclei near $N = Z$

M. Scheck,^{1,2,3,*} V. Yu. Ponomarev,¹ M. Fritzsche,^{1,†} J. Joubert,^{1,‡} T. Aumann,¹ J. Beller,¹ J. Isaak,^{1,4,5} J. H. Kelley,^{6,7} E. Kwan,^{7,8,§} N. Pietralla,¹ R. Raut,^{7,8,||} C. Romig,¹ G. Rusev,^{7,8,¶} D. Savran,^{4,5} L. Schorrenberger,¹ K. Sonnabend,⁵ A. P. Tonchev,^{7,8,§} W. Tornow,^{7,8} H. R. Weller,^{7,8} A. Zilges,⁹ and M. Zweidinger¹

¹*Institut für Kernphysik, Technische Universität Darmstadt, D-64289 Darmstadt, Germany*

²*School of Engineering, University of the West of Scotland, Paisley PA1 2BE, United Kingdom*

³*SUPA, Scottish Universities Physics Alliance, Glasgow G12 8QQ, United Kingdom*

⁴*ExtreMe Matter Institute EMMI and Research Division GSI Helmholtzzentrum für Schwerionenforschung GmbH, D-64291 Darmstadt, Germany*

⁵*Institut für Angewandte Physik, Goethe-Universität Frankfurt, D-60438 Frankfurt am Main, Germany*

⁶*Department of Physics, North Carolina State University, Raleigh, North Carolina 27695-8202, USA*

⁷*Triangle Universities Nuclear Laboratory, Durham, North Carolina 27710, USA*

⁸*Department of Physics, Duke University, Durham, North Carolina 27708-0308, USA*

⁹*Institut für Kernphysik, Universität zu Köln, D-50937 Cologne, Germany*

(Received 9 July 2013; published 7 October 2013)

Background: Within the last decade, below the giant dipole resonance the existence of a concentration of additional electric dipole strength has been established. This accumulation of low-lying $E1$ strength is commonly referred to as pygmy dipole resonance (PDR).

Purpose: The photoresponse of ^{60}Ni has been investigated experimentally and theoretically to test the evolution of the PDR in a nucleus with only a small neutron excess. Furthermore, the isoscalar and isovector $M1$ resonances were investigated.

Method: Spin-1 states were excited by exploiting the (γ, γ') nuclear resonance fluorescence technique with unpolarized continuous bremsstrahlung as well as with fully linearly polarized, quasimonochromatic, Compton-backscattered laser photons in the entrance channel of the reaction.

Results: Up to 10 MeV a detailed picture of $J = 1$ levels was obtained. For the preponderant number of the individual levels spin and parity were firmly assigned. Furthermore, branching ratios, transition widths, and reduced $B(E1)$ or $B(M1)$ excitation probability were calculated from the measured scattering cross sections. A comparison with theoretical results obtained within the quasiparticle phonon model allows an insight into the microscopic structure of the observed states.

Conclusions: Below 10 MeV the directly observed $E1$ strength $[\sum B(E1) \uparrow = (153.8 \pm 9.5) e^2(\text{fm})^2]$ exhausts 0.5% of the Thomas-Reiche-Kuhn sum rule. This value increases to 0.8% of the sum rule $[\sum B(E1) \uparrow = (250.9 \pm 31.1) e^2(\text{fm})^2]$ when indirectly observed branches to lower-lying levels are considered. Two accumulations of $M1$ excited spin-1 states near 8 and 9 MeV excitation energy are identified as isoscalar and isovector $M1$ resonances dominated by proton and neutron $f_{7/2} \rightarrow f_{5/2}$ spin-flip excitations. The $B(M1) \uparrow$ strength of these structures accumulates to $3.94(27)\mu_N^2$.

DOI: [10.1103/PhysRevC.88.044304](https://doi.org/10.1103/PhysRevC.88.044304)

PACS number(s): 23.20.Lv, 21.60.Jz, 25.20.Dc, 27.50.+e

I. INTRODUCTION

In atomic nuclei the total $E1$ strength predicted by the Thomas-Reiche-Kuhn (TRK) sum rule [1] is almost completely concentrated in the giant dipole resonance (GDR) [2]. The geometrical picture visualizes the GDR as an oscillation of all protons against all neutrons. However, experiments using

tagged photons, $^{138}\text{Ba}(\gamma, \gamma')$, and $^{140}\text{Ce}(\gamma, \gamma')$ experiments [3–5] exhibited in these nuclei an extra amount of $E1$ strength between 5 and 8 MeV, an energy region far below the domain of the GDR, which is situated well above 10-MeV excitation energy. Since these first high-resolution γ -ray spectroscopy experiments in the middle of the 1990s, a great deal of experimental work has been performed to investigate the origin of this additional $E1$ strength in several semimagic and some open-shell nuclei across the entire nuclear landscape [6].

The accumulation of 1^- states between 5 and 12 MeV excitation energy with a resonancelike strength distribution is commonly referred to as pygmy dipole resonance (PDR). In a geometrical picture the PDR is often associated with a vibration of the neutron skin against an almost $N \approx Z$ core. The experimental strength of the PDR exhausts up to a few percent of the TRK sum rule. As expected in the geometrical picture the strength seems to exhibit a dependence of the

* marcus.scheck@uws.ac.uk

† Present address: Areva NP GmbH, D-91052 Erlangen, Germany.

‡ Present Address: Ecole Centrale Lyon, 69130 Ecully, France.

§ Present Address: Physics Division, Lawrence Livermore National Laboratory, Livermore, California 94550, USA.

|| Present address: UGC-DAE Consortium for Scientific Research, Kolkata Centre, Kolkata-700098, India.

¶ Present Address: Chemistry Division, Los Alamos National Laboratory, Los Alamos, New Mexico 87545, USA.

ratio of protons and neutrons. However, the experimental data available so far are not conclusive on this [6] and further data are necessary to test whether there are correlations. Also, its nature is still intensely debated, especially the questions of whether the $E1$ strength is linked to the neutron skin and to what extent conclusions about the asymmetry energy can be drawn [7,8].

Among many theories (for an overview, see Ref. [9] and references therein) that are capable of describing the experimentally observed features of the PDR, one of the most successful is the quasiparticle phonon model (QPM) [10]. It describes the mean energy, summed strength, and, in particular, the fragmentation of the PDR to a high level of accuracy. Within this microscopic approach the number of experimentally observed 1^- states cannot be explained considering just $[\alpha_i^\dagger, \alpha_j^\dagger]$ two-quasiparticle excitations. Here, α_i^\dagger and α_j^\dagger denote quasiparticle creation operators. In the particle picture these particular two-quasiparticle excitations can be associated with one-particle, one-hole (1p1h) excitations across a major shell gap. Only the inclusion of multiphonon excitations up to the third phonon order in the model space reproduces the observed degree of fragmentation (e.g., see Refs. [11–13]). The transition densities (TDs) calculated in the QPM framework exhibit nicely the different microscopic structures of the excited 1^- levels, as for example observed in the comparison of $(\alpha, \alpha'\gamma)$ and (γ, γ') experiments [14–18]. The $(\alpha, \alpha'\gamma)$ technique with the isoscalar ($T = 0$) α particle as probe populates only a small fraction of 1^- levels excited in the (γ, γ') reaction. These are especially the low-lying 1^- levels. Their TDs exhibit the oscillation of the excess neutron versus an in-phase motion of protons and core neutrons. In between a crossover region is observed and, as expected for states with a predominant GDR component in the wave function, the TDs of higher-lying levels exhibit an out-of-phase motion of proton and neutron densities.

As already mentioned, multiphonon structures can also lead to 1^- levels, which in some cases are separated from the energy domain of the PDR. The prime example for such an excitation is the quadrupole-octupole coupled $[2_1^+ \otimes 3_1^-]_1$ -state. It is the low-spin member of a quintuplet originating from the coupling of the lowest-lying 2_1^+ quadrupole and 3_1^- octupole phonons. In the past this kind of excitation has been thoroughly studied and an extensive systematics exists [19]. Usually, this heterogeneous $[2_1^+ \otimes 3_1^-]_J$ two-phonon coupling displays only a small degree of anharmonicity and the 1^- level is found close to the sum energy of the 2_1^+ and 3_1^- levels. In spherical or near-spherical nuclei this particular 1^- level is, in general, the lowest-lying negative parity spin-1 level.

There are various experimental methods exploited for the investigation of the above-introduced electric dipole excitations. In radioactive nuclei, such as for example ^{68}Ni [20] and ^{132}Sn [21], relativistic Coulomb excitation has been the method of choice. For the investigation of stable nuclei a whole arsenal of experimental techniques is available, such as the already mentioned $(\alpha, \alpha'\gamma)$ technique exploiting the isoscalar α particles as probe [14,16–18], the (p, p') method [22–25], or the so-called Oslo method (e.g., see Ref. [26]). The latter extracts the γ -ray strength function in the quasicontinuum

region from particle- γ coincidences recorded following light-ion-induced reactions [27,28]. However, the workhorse is the (γ, γ') reaction, the so-called nuclear resonance fluorescence (NRF) technique [29,30]. In NRF experiments real photons are scattered off the nucleus of interest. As the massless real photons transfer almost no momentum, the angular momentum transfer is almost entirely given by the intrinsic angular momentum of $1\hbar$ carried by the incident photon. $E2$ transitions are induced to only a minor extent and other multipolarities such as $M2$, $E3$, etc., do not occur. Hence, NRF is a perfect tool to study selectively spin-1 levels embedded in a sea of states with higher angular momentum. Because the electromagnetic interaction is the only one involved in the scattering process, NRF provides completely model-independent data.

Most of the experiments performed to explore the PDR concentrated on heavier or neutron-rich nuclei with pronounced neutron-to-proton ratios. To study the evolution of the PDR and its dependence on the excess neutrons it is mandatory to perform systematic studies in isotonic and isotopic chains. For example, this has been done using the (γ, γ') technique for the Ca isotopic chain [31–33], the Mo isotopic chain [34], or selected $N = 82$ isotones [4,5,13,21,35–37]. For the latter Coulomb excitation of the unstable ^{132}Sn also was exploited. A more complete overview is given in Ref. [6].

So far in the Ni isotopic chain the stable, almost $N = Z$ isotope ^{58}Ni [38], exploiting the (γ, γ') reaction, and in Coulomb excitation the unstable, neutron-rich isotope ^{68}Ni [20] have been investigated. The intention of this work is to extend the systematics in the Ni isotopic chain by studying ^{60}Ni . Furthermore, we also investigate in detail the evolution of the PDR near the $N = Z$ isospin saturation when adding an additional pair of neutrons to the previously studied ^{58}Ni .

Besides the negative-parity spin-1 levels, the (γ, γ') reaction also excites $J^\pi = 1^+$ states. For example, previous NRF studies in ^{56}Fe and ^{58}Ni [38,39] demonstrated that in the energy region where the PDR is located $M1$ -excited 1^+ levels also can be found. In spherical, semimagic nuclei the $M1$ -strength distribution is dominated by the isoscalar and isovector $M1$ resonances [40]. In the almost $N = Z$ fp -shell nuclei the structure of the resonances is expected to be dominated by 1p1h spin-flip excitations, such as, e.g., $f_{7/2} \rightarrow f_{5/2}$, for protons and neutrons. These 1p1h excitations are mixed coherently by the residual spin-isospin/tensor interaction into an isoscalar and isovector combination. In the $A \approx 60$ mass region the latter resonances are found near 9 MeV excitation energy. Below this energy the debris of the original 1p1h spin-flip excitations is found. Because the Ni isotopes are closed-shell nuclei, no orbital $M1$ strength owing to the $[2_1^+ \otimes 2_{ms}^+]_{1+}$ coupling is expected [30,40,41]. The latter represents a two-phonon excitation of the first excited 2_1^+ level, corresponding to a symmetric coupling of proton and neutron components in the wave function and the so-called mixed-symmetry 2_{ms}^+ state corresponding to an antisymmetric coupling of proton and neutron components. Recently, a $^{90}\text{Zr}(p, p')$ experiment [25] demonstrated that for selected nuclei the $M1$ strength can exhaust a substantial fraction of the dipole strength. A subsequent $^{90}\text{Zr}(\gamma, \gamma')$ study [42] revealed the fine structure of the $M1$ resonances in this nucleus. A similar experimental approach [38,39] as used in this work shed light on the dipole

response of ^{56}Fe . Here, 16 more strongly excited 1^+ levels were observed in the energy range between 6.9 and 10 MeV.

The outline of this paper is as follows. The experimental method, setups, and procedures are introduced in Sec. II. In Sec. III the experimental findings for ^{60}Ni and some additional parity assignments for ^{58}Ni are presented. In Sec. IV the experimental findings are interpreted and compared to calculations within the framework of the QPM. Finally, the work closes with a summary of the experimental findings and the conclusion drawn with the support of the theoretical investigation (Sec. V).

II. EXPERIMENTAL METHOD AND SETUPS

The dipole response of ^{60}Ni was investigated in a series of (γ, γ') measurements using bremsstrahlung with a continuous photon-energy distribution and $(\vec{\gamma}, \gamma')$ measurements using 100% linearly polarized, Compton-backscattered laser photons with a quasimonochromatic energy distribution in the entrance channel. The use of two photon sources, produced via two different reaction mechanisms that complement each other, makes it possible to extract maximum information about the nuclear dipole response in a most efficient way. Of course, this demands the use of different experimental setups at two distinct facilities.

The measurements using bremsstrahlung as primary radiation were performed at the Darmstadt High-Intensity Photon Setup (DHIPS) [43]. An electron beam is accelerated by the injector part of the Superconducting DARMstadt electron LINear ACcelerator (S-DALINAC) and strikes on a massive copper radiator target. Therein the bremsstrahlung is created by converting the kinetic energy of the electrons into radiation. Typical electron currents in the experiment were $20 \mu\text{A}$. The initial kinetic electron energies, which correspond to the maximum photon energy of the bremsstrahlung spectrum, were 6.0, 8.0, and 9.9 MeV. The energies were chosen to minimize feeding effects in low-lying levels and shift the region of maximum sensitivity. The latter is given as a combination of the photon flux, detector efficiency, and the background in the γ -ray spectra. Because the incident photons interact with the atomic system rather than with the nucleus, the NRF technique suffers from a massive background exponentially growing at lower energies. This drawback often prevents the observation of weak γ -ray branches to lower-lying excited states or the observation of weakly excited states. As sensitivity limit it was required that the area of a peak to be accepted as such exceeded two standard deviations of the background underneath in at least two of three recorded spectra.

The scattering sample for the bremsstrahlung measurements consisted of 2.996 g of metallic Ni enriched to 99.8% in the isotope ^{60}Ni . Three high-purity germanium (HPGe) detectors, each with 100% relative efficiency (relative to a $3'' \times 3''$ NaI detector), were placed under angles of 90° and 130° with respect to the incident photon beam. The detectors were embedded in a massive lead shielding and each was equipped with a bismuth-germanate-oxide (BGO) active anti-Compton shielding. For the 6.0 and 8.0 MeV measurements the target was sandwiched between disks of enriched (99.8%)

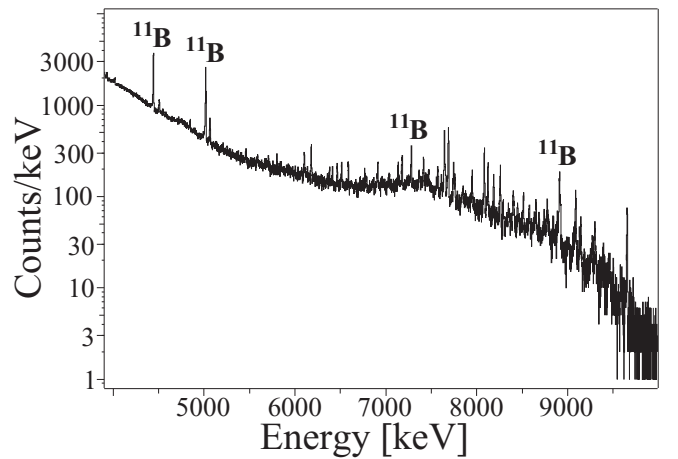


FIG. 1. Partial $^{60}\text{Ni}(\gamma, \gamma')$ spectrum recorded at DHIPS at the S-DALINAC facility. The energy of the incident electrons and, therefore, the photon-flux end-point energy was 9.9 MeV. Peaks labeled with ^{11}B stem from the corresponding isotope used for photon flux normalization. The spectrum includes, besides the full-energy peaks, peaks stemming from single- and double-escape events and background lines. An extended part of this spectrum is shown in part (d) of Fig. 2. Note that the y axis is plotted in logarithmic scale.

^{11}B and for the 9.9-MeV measurement between disks of natural boron. The well-known and documented decays of the photoexcited levels of ^{11}B [44] serve as the calibration standard for the flux of the incident photons.

The relative detector efficiency for energies up to 10 MeV was simulated using the GEANT4 toolkit [45]. In the low-energy regions the efficiency curves were adjusted to experimental values obtained with a ^{56}Co calibration source. This procedure accounts for the different opening angles and intrinsic efficiencies of the detectors in use. An exemplary spectrum as recorded at DHIPS with $E_{e^-} = 9.9$ MeV is illustrated in Fig. 1.

The angular distributions of the two elastic cascades possible for an even-even nucleus in NRF, $0^+ \rightarrow 1^\pi \rightarrow 0^+$ and $0^+ \rightarrow 2^+ \rightarrow 0^+$, exhibit a large difference at scattering angles of 90° and 127° . It has to be mentioned that in NRF the term “elastic” denotes a scattering process with excitation from the ground state and a decay directly back to the ground state. The term “inelastic” denotes a scattering process starting from the ground state as well but in which the decay process happens via a cascade including lower-lying excited states. Knowing the efficiency ratios of two detectors, the ratio of their angular distributions, $W(\theta)$, of a given γ -ray transition can be determined experimentally as

$$\frac{W(90^\circ)}{W(130^\circ)} = \frac{A_\gamma(90^\circ)\epsilon(E_\gamma, 130^\circ)}{A_\gamma(130^\circ)\epsilon(E_\gamma, 90^\circ)}. \quad (1)$$

Into Eq. (1), enter the efficiencies $\epsilon(E_\gamma, \theta)$ and dead-time corrected peak intensities $A_\gamma(\theta)$ measured in the detectors placed at the angles θ . This ratio can be compared to the theoretical values for a given spin sequence $0^+ \rightarrow J^\pi \rightarrow J_f^{\pi_f}$. The corresponding values are given in Table I. For their calculation the phase convention of Rose and Brink [46] was used. Furthermore, it has to be mentioned that feeding

TABLE I. Calculated $W(90^\circ)/W(130^\circ)$ ratios of the angular distributions using the angles as realized in the bremsstrahlung-beam experiment at DHIPS for the cascades observed in this experiment. In case a transition multipolarity allows for $E2/M1$ multipole mixing, the values for the most extreme multipole-mixing parameters δ are given. When calculating the ratios for the multipole-mixing ratios the phase convention of Rose and Brink [46] was used.

Cascade	δ	$W(90^\circ)/W(130^\circ)$
$0^+ \rightarrow 1^\pi \rightarrow 0^+$		0.708
$0^+ \rightarrow 1^\pi \rightarrow 2^+$	0	0.920
$0^+ \rightarrow 1^+ \rightarrow 2^+$	∞	0.853
$0^+ \rightarrow 2^+ \rightarrow 0^+$		2.253
$0^+ \rightarrow 2^+ \rightarrow 2^+$	0	0.850
$0^+ \rightarrow 2^+ \rightarrow 2^+$	∞	1.365

into a level via a multi- γ -ray cascade drives the ratio of its depopulating transitions towards unity.

The cross section $I_{S,f}$ for the scattering process to a final state f , in dependence on the quantities observed in the experiment, is given as

$$I_{S,f} = \frac{A_\gamma}{N_t \epsilon(E_\gamma) N_\gamma(E_R) W(\theta)}. \quad (2)$$

Here, A_γ denotes the peak area taken from the spectrum, N_t the number of target nuclei, $\epsilon(E_\gamma)$ the detector efficiency, $N_\gamma(E_R)$ the photon flux at the resonance energy E_R , and $W(\theta)$ the angular distribution considering the geometry realized in the experiment. Because ^{11}B is used as calibration standard, there is only a need to determine the relative efficiency. As mentioned before, the spectroscopic properties of the γ -ray transitions of ^{11}B [44,47] emitted after photoexcitation are known to a high level of precision. In order to minimize systematic uncertainties, the scattering cross sections of the isotope of interest are determined relative to those of the reference isotope ^{11}B .

The experimentally determined scattering cross section $I_{S,f}$,

$$I_{S,f} = \pi^2 \left(\frac{\hbar c}{E_R} \right)^2 \frac{(2J_R + 1)}{(2J_0 + 1)} \cdot \Gamma_0 \frac{\Gamma_f}{\Gamma}, \quad (3)$$

is proportional to the ground-state decay width, Γ_0 , describing the excitation path. The deexcitation path is accounted for by the ratio of the partial decay width, Γ_f , to the final level f and the total decay width, Γ . Furthermore, a statistical factor $(2J_R + 1)/(2J_0 + 1)$ counting over the number of magnetic substates involved in the scattering process and the reduced scattering wavelength $\lambda = (\hbar c)/E_R$ enter the equation. The total decay width, Γ , corresponds to the sum of all partial decay widths of the photoexcited level ($\Gamma = \sum_{f=0} \Gamma_f$). Via the time-energy-uncertainty relation Γ is inverse proportional to the lifetime, $\tau = \hbar/\Gamma$, of the excited level. However, as previously mentioned, NRF suffers especially at low energies from the huge nonresonant atomic background. Therefore, weak or low-energy γ -ray transitions are usually not observed. This results for many levels in an underestimation of the total decay width and consequently an overestimation of the level lifetime. Furthermore, feeding into a level increases

the measured scattering cross sections and, therefore, obscures the decay widths and lifetime.

Particularly interesting for the aims of this project is the determination of reduced ground-state excitation probabilities $B(\Pi L, 0^+ \rightarrow J^\pi) = B(\Pi L) \uparrow$. These are directly related to the reduced ground-state decay width $\Gamma_0^{\text{red}} = \Gamma_0/E_\gamma^{(2L+1)}$ of the level

$$B(\Pi L) \uparrow = C_{\Pi L} (2J_R + 1) \frac{\Gamma_0}{E_R^{2L+1}}. \quad (4)$$

When Γ_0^{red} is entered in units of $\text{meV}/\text{MeV}^{(2L+1)}$ the coefficients $C_{\Pi L}$ for the possible multiplicities ($C_{E1} = 0.955 \times 10^{-3}$, $C_{M1} = 0.08643$, and $C_{E2} = 1.245 \times 10^3$) result in corresponding units of $e^2(\text{fm})^{2L}$ for electric and μ_N^2 for magnetic transitions, respectively.

A second experiment with the aim of measuring the parities of the excited spin-1 states was conducted at the Duke Free Electron Laser Laboratory (DFELL) at the Triangle Universities Nuclear Laboratory (Durham, NC, USA). A detailed description of the facility can be found in Ref. [48]. This facility is capable of providing a quasimonochromatic beam of fully linearly polarized photons in the entrance channel of the $(\vec{\gamma}, \gamma')$ reaction. To produce these beams electron bunches are accelerated exploiting the 240-MeV linac and injected into the 1.2-GeV storage ring. In the storage ring an electron bunch is forced to emit light in a wiggler system of a free-electron laser (FEL). These FEL photons with typical energies in the electron volt range are reflected from a mirror approximately 27 m from the collision point. The reflected beam is then Compton backscattered at a second circulating electron bunch. The Compton-backscattering process not only preserves the well-defined polarization vector of the FEL photons but also boosts their energy into the MeV range. The variation of the electron energies allows for a tuning of the resulting γ -ray energies. For the Compton-backscattered photons in the MeV range the mirror system is almost perfect. Hence, they are decoupled from the production facility and approximately 60 m downstream of the collision point a massive lead collimator selects for a small angular range, corresponding to a well-defined energy range of the Compton-backscattered photons. The resulting energy spread of the photon flux can be adjusted by the use of collimator holes with a variable diameter.

The procedure described above results in quasimonochromatic, fully linearly polarized photon beams in the entrance channel of the $(\vec{\gamma}, \gamma')$ reaction. Applying the formalism outlined in Ref. [49], the angular distribution, $W(\theta, \phi)$, of the resonantly scattered photons for a spin-1 state ($0^+ \rightarrow 1^\pi \rightarrow 0^+$) is calculated as

$$W(\theta, \phi) = \frac{3}{2} + \frac{3}{4}(1 - \cos^2 \theta)(\pi \cos 2\phi - 1). \quad (5)$$

Obviously, the scattering process in NRF exploiting fully polarized photon beams shows at a polar angle of $\theta = 90^\circ$ a strong azimuthal (ϕ angle) dependence on the parity, π , of the excited spin-1 state. Hence, this method is a perfect tool to determine the parity. The momentum ($\theta = 0^\circ, \phi = 0^\circ$) and polarization ($\theta = 90^\circ, \phi = 0^\circ$) vectors of the incident photons define the so-called polarization plane (PP). The scattering for a positive/negative-parity spin-1 level happens

within/perpendicular to the PP. Thus, the theoretical analyzing power, Σ , can be defined as

$$\begin{aligned}\Sigma &= \frac{W(90^\circ, 0^\circ) - W(90^\circ, 90^\circ)}{W(90^\circ, 0^\circ) + W(90^\circ, 90^\circ)} \\ &= \begin{cases} +1 & \text{for } J^\pi = 1^+, \\ -1 & \text{for } J^\pi = 1^-. \end{cases} \end{aligned} \quad (6)$$

Consequently, for an $M1$ -excited level a maximum is measured at angle combinations $(\theta_{M1}, \phi_{M1}) = (90^\circ, 0^\circ)$ and $(90^\circ, 180^\circ)$ and for an $E1$ -excited level at angles of $(\theta_{E1}, \phi_{E1}) = (90^\circ, 90^\circ)$ and $(90^\circ, 270^\circ)$. Hence, these angle combinations are the most sensitive for a parity determination. However, in an experiment the finite opening angles of the detectors diminish the perfect ratio of Eq. (6). Therefore, the experimental asymmetry, A_{exp} , is defined as the product of the analyzing power, Σ , and the experimental sensitivity, Q ,

$$A_{\text{exp}} = Q\Sigma = \frac{A_{\parallel}/t_{\parallel} - (\epsilon_{\parallel}/\epsilon_{\perp})A_{\perp}/t_{\perp}}{A_{\parallel}/t_{\parallel} + (\epsilon_{\parallel}/\epsilon_{\perp})A_{\perp}/t_{\perp}}. \quad (7)$$

The experimental quantities A_{\parallel} and A_{\perp} denote the peak areas in the spectra recorded within and perpendicular to the PP, respectively. Furthermore, the lifetimes, t_i ($i = \perp$ or \parallel), corrected for the electronics dead time and the efficiency ratio $\epsilon_{\parallel}/\epsilon_{\perp}$ of the detector systems within and perpendicular to the PP are accounted for. Examples for spectra recorded in the ^{60}Ni experiment are presented in Fig. 2. Figure 2(b) shows a spectrum recorded at $\text{HI}\bar{\gamma}\text{S}$ within the PP and Fig. 2(c) a spectrum recorded perpendicular to the PP. Despite the low background in the energy range covered by the incident photon beam, often transitions of weakly populated levels are exclusively visible in only one of the two spectra. In this part of the experiment, a sensitivity limit of five standard deviations of the Poisson-distributed background was required for a peak to be accepted as such. In Fig. 2 only the strongly populated 9092.6-keV level has corresponding peaks in both spectra. Nevertheless, the observed asymmetry clearly favors a $J^\pi = 1^-$ assignment to this level. In most cases the peak in the perpendicular detector resulting from the finite opening-angle effect is too weak to be distinguished from the background. Because of its very sensitive polarimeter properties, the setup can also be used to disentangle multiplets of overlapping peaks stemming from levels with different parities. This is demonstrated in Fig. 2 as well (dashed line). In the bremsstrahlung spectrum [Fig. 2(d)] the enhanced width of the peak at ≈ 9305 keV already indicated the presence of a doublet. In Figs. 2(b) and 2(c) two peaks clearly shifted in energy are visible.

In a previous publication the advantage of quasimonoenergetic beams over bremsstrahlung beams has been highlighted [50]. The quasimonoenergetic beam results were compared to bremsstrahlung beams in less nonresonant scattered background in the low-energy part of the spectrum. Also, as demonstrated in Figs. 2(b) and 2(c), the region covered by the beam suffers from less background compared to a bremsstrahlung spectrum [Fig. 2(d)] recorded at DHIPS and, therefore, has an improved peak-to-background ratio. However, in this campaign in the intermediate region down to $\approx 50\%$ of the energy under consideration the bremsstrahlung spectra had a better peak-to-background ratio. This is at-

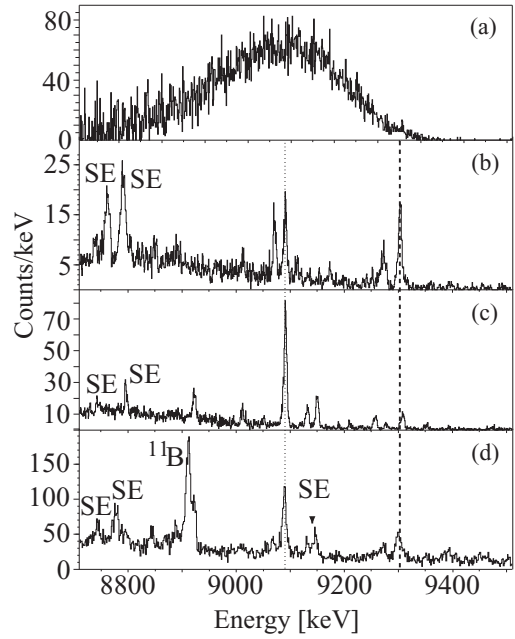


FIG. 2. Spectral distribution of the photon flux in the $\bar{E}_\gamma = 9110$ MeV measurement at the $\text{HI}\bar{\gamma}\text{S}$ facility (a), the $(\bar{\gamma}, \gamma')$ spectra recorded at $\text{HI}\bar{\gamma}\text{S}$ within (b) and perpendicular to (c) the polarization plane (PP), and the corresponding part of a (γ, γ') spectrum recorded at DHIPS ($E_{e^-} = 9.9$ MeV) using unpolarized bremsstrahlung (d). Transitions appearing in the spectrum recorded in/perpendicular to the PP are of $M1/E1$ character. Peaks belonging to ^{11}B and single-escape (SE) events are labeled as such. The dashed line indicates a peak that was unfolded using the information from $\text{HI}\bar{\gamma}\text{S}$, while the dotted line shows an example for a strong transition with sufficient statistics to appear in both $\text{HI}\bar{\gamma}\text{S}$ spectra. Note the different scaling of the y axis.

tributable to the absence of active anti-Compton shields in the $\text{HI}\bar{\gamma}\text{S}$ measurements.

In this campaign three different setups at $\text{HI}\bar{\gamma}\text{S}$ and various mean photon-flux energies were used. Almost the entire energy region between 6 and 10 MeV excitation energy was covered and for most of the observed dipole excited states firm parity assignments were made. The major setup [50] consisted of four HPGe detectors in crosslike geometry at polar angles of 90° with respect to the incident beam. Two detectors were situated at azimuthal angles corresponding to the PP ($\phi = 0^\circ$ and 180°) and two detectors perpendicular to the PP ($\phi = 90^\circ$ and 270°). Each detector had an intrinsic efficiency of 60%. The target sample was the identical 2.996-g metallic sample enriched to 99.8% in ^{60}Ni as used in the DHIPS measurements. A ^{56}Co -source calibration was used to determine the efficiency ratio of the detectors in the two main scattering directions. A simulated efficiency curve, obtained with the GEANT toolkit [45], was adjusted to the experimental ^{56}Co values. As outlined in Ref. [50], indirect evidence for the branching behavior of the excited spin-1 states was observed. The depopulation of low-lying levels in an energy region far off the energy of the incident beam provided information about the summed-up feeding from the primarily excited spin-1 levels in the energy range covered by the incident photons. Furthermore, a second setup approximately 2 m upstream of the above-described

setup employing two Clover detectors at $(\theta, \phi) = (90^\circ, 0^\circ)$ and $(90^\circ, 90^\circ)$ was used. This setup was operated parasitically, while the major setup was used for the investigation of other nuclei. The positioning behind another NRF target resulted in a less intense, but still usable, beam. In these measurements a Ni sample of natural composition was used. This resulted in additional parity information for the more naturally abundant (68.1%) ^{58}Ni (^{60}Ni : 26.2%).

III. EXPERIMENTAL RESULTS

In this section the experimental results are presented. For the assignment of ground-state decays, the information obtained in the $\text{HI}\bar{\gamma}\text{S}$ spectra was used. If a transition appeared in the energy range covered by the photon beam, it was seen as such. Additional peaks in the DHIPS spectra were assigned to the levels, as transitions connecting those to lower-lying excited levels, using the Ritz variation principle. Therefore, the recoil-corrected transition energy was added to the known energies of the lower-lying levels of ^{60}Ni [44] to determine whether a ground-state transition corresponds to the sum. Basically, the ratio of the angular distribution could serve as a check for this procedure (see Table I) but, unfortunately, in most cases the transitions to lower-lying levels are weak and the corresponding $W(90^\circ)/W(130^\circ)$ ratios close to each other. Consequently, within two standard deviations no firm conclusion can be drawn.

The angular distribution ratios [Eq. (1)] were used to assign the spins. In order to minimize feeding effects (see Fig. 4) the measurement with 6.0 MeV end-point energy was used up to 5.1 MeV, between 5.8 and 7.5 MeV a combination of the 8.0- and 9.9-MeV end-point energy measurements was exploited, and above that only the 9.9 MeV measurement was employed. The corresponding values for all observed γ -ray transitions are illustrated in Fig. 3. The observed ratios allowed for a firm spin assignment of 69 states. Apart from the level at 6229 keV, all levels above 5.0 MeV are assigned to have $J = 1$.

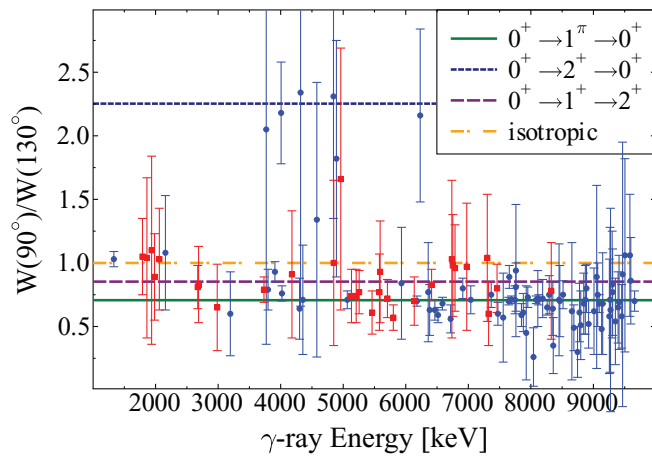


FIG. 3. (Color online) Ratio $W(90^\circ)/W(130^\circ)$ for the observed γ -ray transitions as determined in the DHIPS experiments. Theoretical values are represented as (dashed) lines. Assigned ground-state transitions are marked with the (blue) circles. Transitions associated with decays to lower-lying states are indicated by (red) squares. For a more detailed discussion see text.

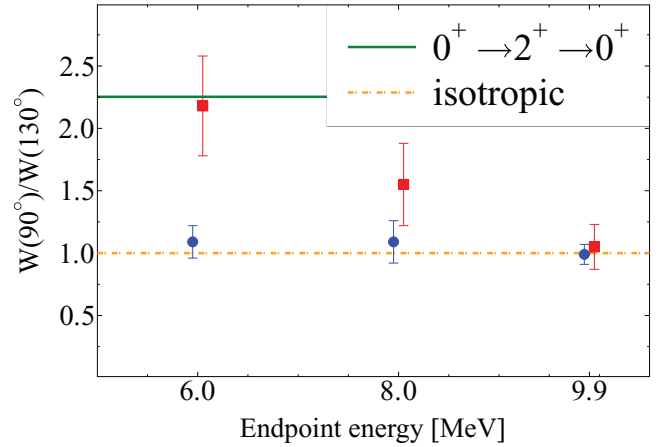


FIG. 4. (Color online) Ratio $W(90^\circ)/W(130^\circ)$ as observed for the ground-state decays of first excited 2^+ level at 1332.4 keV (blue circles) and a 2^+ level at 4007.9 keV (red squares) in dependence on the photon-flux end-point energy. The theoretical values are shown as dashed lines. While the first 2^+ level receives feeding from higher-lying levels at all end-point energies, the angular distribution ratio for the level at 4007.9 keV exhibits a gradually increasing feeding. For a clarity of the presentation the points were slightly offset from their end-point-energy values.

As mentioned previously, the angular distribution ratios exhibit the degree to which the corresponding level was fed. Examples are shown in Fig. 4. In this figure the ratios $W(90^\circ)/W(130^\circ)$ of the ground-state decay for the first excited 2^+ level at 1332.4 keV (blue circles) and a 2^+ level at 4006.7 keV (red squares) are illustrated in dependence on the end-point energy of the incident photon flux. Obviously, the first 2^+ level has an isotropic angular distribution for all end-point energies used, a fact that clearly indicates strong feeding for all measurements. The level at 4006.7 keV receives feeding from levels above 6.0 MeV excitation energy. Furthermore, for levels which were observed only in the $\text{HI}\bar{\gamma}\text{S}$ measurements, the spin assignment is firm if they are $E1$ excited. When they are exclusively observed in the spectra recorded within the PP, it is far more likely that they are spin-1 levels than spin-2. As demonstrated in Figs. 2(b) and 2(c) the parities could be assigned straightforwardly from the spectra recorded at $\text{HI}\bar{\gamma}\text{S}$.

The quantities related to the transition probabilities were calculated according to Eqs. (2)–(5). Because for the 8.0-MeV measurement at DHIPS the mass of the boron calibration standard was not determined precisely, this measurement could be used only to determine further branches to lower-lying excited states and to improve the accuracy of the angular distribution. However, a comparison of the angular distribution ratios observed for the 8.0- and 9.9-MeV measurement did not indicate a feeding into levels above 5 MeV excitation energy. Therefore, the use of only the 9.9-MeV measurement can be seen as justified. Furthermore, the integrated cross sections were cross checked with previously measured data [52] and the data obtained in the 9.9-MeV measurement showed a good agreement. In some cases the parity-sensitive scattering of the $\text{HI}\bar{\gamma}\text{S}$ data provided information about doublets not resolvable in the bremsstrahlung experiments. The peak areas in the DHIPS spectra were divided into an $E1$ and a $M1$ part

TABLE II. Nuclear data information observed for $J^\pi = 1^-$ levels in ^{60}Ni . Given are the level energy, E_R , and γ -ray energy, E_γ , of the depopulating transitions, the energy of the final level, E_f , spin and parity of the final level, J_f^π , the integrated cross section, $I_{S,f}$, the branching ratio, Γ_f/Γ , the ground-state width, Γ_0 , the level lifetime, τ , as calculated from Γ , and the reduced ground-state excitation probability, $B(E1, 0^+ \rightarrow 1^-)$.

E_R (keV)	E_γ (keV)	E_f^a (keV)	$J_f^\pi^a$	$I_{S,f}$ (eV b)	Γ_f/Γ	Γ_0 (meV)	τ (fs)	$B(E1, 0^+ \rightarrow 1^-)$ ($10^{-3} e^2(\text{fm})^2$)
6180.6(6)	6180.6(7) 4848.4(14)	0 1332.5	0^+ 2_1^+	64.1(84) 6.5(27)	0.91(1) 0.09(4)	234(34)	2.6(4)	2.84(41)
6382.2(10)	6382.2(10) ^b	0	0^+	10.4(27)	1	37(10)	18.0(47)	0.40(11)
6465.2(6)	6465.2(9) 5131.6(10) ^c 4180.5(14)	0 1332.5 2284.9	0^+ 2_1^+ 0_2^+	27.8(46) 7.8(22) 10.4(38)	0.60(4) 0.17(4) 0.23(7)	167(39)	2.4(7)	1.77(42)
6587.6(6)	6587.6(8) 5254.7(10) 4302.0(11) ^d	0 1332.5 2284.9	0^+ 2_1^+ 0_2^+	43.8(63) 8.8(21) 13.1(28)	0.67(2) 0.13(4) 0.20(4)	248(43)	1.8(4)	2.48(43)
6718.1(10)	6718.1(10)	0	0^+	17.6(35)	1	69(14)	9.6(19)	0.65(13)
7038.7(7)	7038.7(10) 5705.6(9)	0 1332.5	0^+ 2_1^+	30.0(54) 19.5(36)	0.61(4) 0.39(5)	212(54)	1.9(6)	1.75(44)
7559.0(8)	7559.0(8)	0	0^+	14.2(48)	1	70(24)	9.4(32)	0.47(16)
7646.9(7)	7646.9(7)	0	0^+	330(39)	1	1671(198)	0.39(5)	10.7(13)
7690.9(6)	7690.9(7) 6358.8(16)	0 1332.5	0^+ 2_1^+	406(48) 9.7(30)	0.98(1) 0.02(1)	2133(256)	0.30(4)	13.4(16)
7746.9(5)	7747.3(8) ^e 6413.8(9) 5590.1(10) ^e 5461.9(11)	0 1332.5 2158.6 2284.9	0^+ 2_1^+ 2_2^+ 0_2^+	47.9(91) 23.4(44) 7.5(20) 9.5(21)	0.54(4) 0.27(3) 0.09(1) 0.11(2)	460(121)	0.8(3)	2.83(75)
8085.5(5)	8085.7(7) 6752.3(13) 5800.8(8)	0 1332.5 2284.9	0^+ 2_1^+ 0_2^+	263(32) 19.4(52) 43.6(74)	0.81(2) 0.06(2) 0.13(2)	1848(270)	0.29(5)	10.0(15)
8126.0(7)	8126.0(7)	0	0^+	178(23)	1	1021(131)	0.65(8)	5.45(70)
8188.5(7)	8188.5(7) ^b	0	0^+	75(12)	1	436(68)	1.5(3)	2.27(36)
8260.9(8)	8260.9(8)	0	0^+	191(25)	1	1131(152)	0.58(8)	5.75(77)
8293.7(7)	8293.0(10) 6135.5(11)	0 2158.6	0^+ 2_2^+	41.6(76) 22.8(49)	0.65(4) 0.35(5)	384(95)	1.1(4)	1.93(48)
8406(4) ^f	8406(4)	0	0^+	24(14)	1	72(43)	9.1(54)	0.35(21)
8450.9(16)	8450.9(16) ^b	0	0^+	32.7(73)	1	203(45)	3.3(8)	0.96(22)
8463.4(13)	8463.4(13)	0	0^+	27.3(67)	1	169(42)	3.9(10)	0.80(20)
8514.6(9)	8514.6(9)	0	0^+	101(16)	1	637(103)	1.0(2)	2.96(48)
8654.7(9)	8654.7(9) ^b	0	0^+	54(11)	1	348(69)	1.9(4)	1.54(31)
8746.3(12)	8746.3(12)	0	0^+	74(16)	1	493(107)	1.3(3)	2.11(46)
8780.9(10)	8780.9(10) ^b	0	0^+	55(14)	1	367(94)	1.8(5)	1.55(40)
8923.4(10)	8923.4(10)	0	0^+	185(34)	1	1275(232)	0.52(9)	5.14(94)
9009.8(19)	9009.8(19)	0	0^+	29.8(96)	1	210(67)	3.1(10)	0.82(26)
9052.6(24)	9052.6(24)	0	0^+	22.2(92)	1	158(65)	4.2(17)	0.61(25)
9092.7(8)	9091.2(8) 7761.2(19) ^g	0 1332.5	0^+ 2_1^+	306(44) 76(25)	0.80(2) 0.20(6)	2735(474)	0.19(4)	10.4(18)
9131.5(15)	9131.5(15)	0	0^+	72(16)	1	517(113)	1.3(3)	1.95(42)
9148.7(30)	9148.7(30) ^e	0	0^+	87(38)	1	633(278)	1.0(5)	2.4(11)
9255.2(25)	9255.2(25)	0	0^+	40(18)	1	293(130)	2.2(10)	1.06(47)

TABLE II. (*Continued.*)

E_R (keV)	E_γ (keV)	E_f^a (keV)	$J_f^{\pi^a}$	$I_{s,f}$ (eV b)	Γ_f/Γ	Γ_0 (meV)	τ (fs)	$B(E1, 0^+ \rightarrow 1^-)$ ($10^{-3} e^2(\text{fm})^2$)
9265.7(24)	9265.7(24)	0	0 ⁺	44(21)	1	329(156)	2.0(10)	1.19(56)
9273.9(15)	9273.9(15) ^b	0	0 ⁺	23(17)	1	174(126)	3.8(27)	0.63(45)
9307.5(14)	9307.5(14)	0	0 ⁺	128(48)	1	964(361)	0.7(3)	3.4(13)
9351.8(21)	9351.8(21)	0	0 ⁺	32(15)	1	243(111)	2.7(12)	0.85(39)
9394.7(15)	9394.7(15)	0	0 ⁺	73(28)	1	559(210)	1.2(5)	1.93(73)
9409.9(17)	9409.9(17)	0	0 ⁺	51(21)	1	391(164)	1.7(7)	1.34(56)
9464.5(11)	9464.5(15) ^b 7303.2(16) ^h	0 1332.5	0 ⁺ 2 ₁ ⁺	39(19) 64(19)	0.38(12) 0.62(18)	798(637)	0.3(3)	2.7(22)
9504.1(17)	9504.1(17)	0	0 ⁺	61(25)	1	481(196)	1.4(6)	1.60(66)
9598.2(15)	9598.2(15)	0	0 ⁺	89(33)	1	712(263)	0.9(4)	2.31(85)
9640.0(21) ⁱ	9639.4(2)	0	0 ⁺	18(16)	1	149(126)	4.4(38)	0.48(40)
9658.5(8)	9658.5(9) 8326.0(16)	0 1332.5	0 ⁺ 2 ₁ ⁺	963(240) 111(33)	0.90(2) 0.10(3)	8687(2388)	0.07(2)	27.6(76)
9700.6(15) ⁱ	9700.6(15)	0	0 ⁺	66(37)	1	538(299)	1.2(7)	1.69(94)
9720.2(18) ⁱ	9720.2(18)	0	0 ⁺	44(27)	1	357(219)	1.8(11)	1.11(68)
9750.6(23) ⁱ	9750.6(23)	0	0 ⁺	13(12)	1	111(95)	6.0(51)	0.34(29)
9773.9(20) ⁱ	9773.9(20)	0	0 ⁺	29(20)	1	237(169)	2.8(20)	0.73(52)
9806.6(19) ⁱ	9806.6(19)	0	0 ⁺	35(23)	1	288(192)	2.3(15)	0.87(58)
9831.1(21) ⁱ	9831.1(21)	0	0 ⁺	42(19)	1	354(162)	1.9(9)	1.07(49)
9870.4(20) ⁱ	9870.4(20)	0	0 ⁺	72(51)	1	609(432)	1.1(8)	1.8(13)
9892.6(17) ⁱ	9892.6(17)	0	0 ⁺	114(71)	1	971(600)	0.7(4)	2.9(18)

^aData taken from Ref. [44].^bHI γ S data indicate $M1/E1$ doublet.^cAlternative placement: $7415 \rightarrow 0_2^+$.^dBranch seen only in $E_{e^-} = 8.0$ -MeV measurement.^ePeak contaminated by a single-escape peak.^fDHIPS: Peak covered by single-escape peak, exclusively HI γ S data used.^gDoublet with $7760 \rightarrow 0^+$, branching ratio from HI γ S measurement.^hAssigned to $J^\pi = 1^-$ level because of better agreement in energy.ⁱLevel exclusively observed in HI γ S data.

according to the intensity ratio determined from the HI γ S spectra. The same procedure was applied for some peaks that were in the bremsstrahlung beams either doublets with or entirely covered by single-/double-escape peaks. Furthermore, the spectra recorded at HI γ S revealed some ground-state transitions from levels that were in the DHIPS measurement below the sensitivity limit. The scattering cross section of these levels was determined relative to the strongly excited level at 9658.5 keV. To obtain the necessary spectral distribution of the photon flux the detector response was unfolded from a spectrum measured with a HPGe detector placed in the incident photon beam ($\Theta = 0^\circ$). For the unfolding procedure a script based on GEANT4 [45] was used. An example of such a flux obtained after the unfolding procedure is shown in Fig. 2(a). The resulting values for levels that were observed in both measurements but not used as a cross-normalization point

showed a good agreement. Nevertheless, this procedure results in comparably large errors.

Spin-1 levels that have been assigned with either a negative or a positive parity or whose parity was already known [44] are listed in Tables II and III, respectively. Spin-1 levels for which no parity could be assigned are presented in Table IV. Levels for which a spin and parity assignment of $J^\pi = 2^+$ was made or had already entered the NNDC database [44] are listed in Table V. The lifetimes τ of the individual levels as given in these tables were calculated from the corresponding total decay width Γ .

In the 9.9-MeV measurement the exclusive occurrence of γ rays depopulating lower-lying excited levels indicates that their population predominantly stems from levels between 8 and 9.9 MeV excitation energy. Apart from the $J^\pi = 1^+$ level at 3194 keV and the $J^\pi = 2^+$ levels for which

TABLE III. Nuclear data information observed for $J^\pi = 1^+$ levels in ^{60}Ni . Given are the level energy, E_R , and γ -ray energy, E_γ , of the depopulating transitions, the energy of the final level, E_f , spin and parity of the final level, J_f^π , the integrated cross section, $I_{S,f}$, the branching ratio, Γ_f/Γ , the ground-state width, Γ_0 , the level lifetime, τ , as calculated from Γ , and the reduced ground-state excitation probability, $B(M1, 0^+ \rightarrow 1^+)$.

E_R (keV)	E_γ (keV)	E_f^a (keV)	$J_f^\pi^a$	$I_{S,f}$ (eV b)	Γ_f/Γ	Γ_0 (meV)	τ (fs)	$B(M1, 0^+ \rightarrow 1^+)$ ($10^{-3}\mu_N^2$)
3193.6(7) ^b	3193.3(10)	0	0 ⁺	<4.4(14) ^c	0.16(1) ^d	0.024(8)	>4.5(17)	<190(67)
	1861.2(11)	1332.5	2 ₁ ⁺	<11.1(36)	0.38(1) ^d			
4020.6(3) ^{e,f}	4020.6(3)	0	0 ⁺	8.2(7)	0.55(3) ^d	20(8)	18.4(80)	79(18)
6382.2(10)	6382.2(10) ^g	0	0 ⁺	10.4(27)	1	37(10)	18.0(47)	37(10)
6514.6(9)	6514.6(9)	0	0 ⁺	40.6(62)	1	150(23)	4.4(7)	140(21)
6913.7(7)	6913.7(8)	0	0 ⁺	64.4(97)	0.93(1)	288(47)	2.1(4)	226(37)
	5581.0(18)	1332.5	2 ₁ ⁺	5.1(21)	0.07(3)			
7473.7(9)	7473.7(9)	0	0 ⁺	44.2(75)	1	214(36)	3.1(5)	1.47(25)/133(23)
7657.1(8)	7657.1(8)	0	0 ⁺	93(14)	1	475(70)	1.4(2)	274(40)
7761.6(8)	7761.6(8) ^h	0	0 ⁺	53(13)	1	276(69)	2.4(6)	153(38)
7849.7(10)	7849.7(10)	0	0 ⁺	52.4(87)	1	280(46)	2.4(4)	150(25)
7879.8(12)	7879.8(12)	0	0 ⁺	32.7(67)	1	176(36)	3.7(8)	93(19)
7926.1(17)	7926.1(17)	0	0 ⁺	10.1(45)	1	55(24)	11.9(52)	29(13)
7951.2(2)	7951.2(8)	0	0 ⁺	108(16)	1	590(86)	1.1(2)	304(44)
8042.0(16)	8042.0(16)	0	0 ⁺	10.5(38)	1	59(21)	11.1(41)	29(11)
8111.2(12)	8111.2(12)	0	0 ⁺	27.0(61)	1	154(35)	4.3(10)	75(17)
8188.5(8)	8188.5(8) ^g	0	0 ⁺	46.9(88)	1	273(51)	2.4(5)	129(24)
8351.2(13)	8351.2(13)	0	0 ⁺	31.7(74)	1	192(45)	3.4(8)	85(20)
8358.7(15)	8358.7(15)	0	0 ⁺	22.3(71)	1	135(43)	4.9(16)	60(19)
8450.9(16)	8450.9(16) ^g	0	0 ⁺	16.1(57)	1	100(35)	6.6(23)	43(15)
8655.9(7)	8655.9(9) ^g	0	0 ⁺	32(14)	0.57(11)	363(231)	1.0(9)	145(92)
	7324.2(14)	1332.5	2 ₁ ⁺	24.2(66)	0.43(7)			
8687.7(13)	8687.7(13)	0	0 ⁺	26.8(67)	1	176(44)	3.8(10)	69(17)
8767(4)	8767(4) ⁱ	0	0 ⁺	8.8(88)	1	59(59)	11(11)	23(23)
8777.9(10)	8777.9(10) ^g	0	0 ⁺	54(14)	1	361(93)	1.8(5)	138(36)
8795.2(9)	8795.2(16) ^j	0	0 ⁺	48(19)	0.45(10)	712(444)	1.6(5)	271(169)
	7459.5(11)	1332.5	2 ₁ ⁺	58(12)	0.55(11)			
8845.8(14)	8845.8(14)	0	0 ⁺	45(12)	1	308(76)	2.1(6)	115(29)
8871.0(16)	8871.0(16)	0	0 ⁺	43(11)	1	290(76)	2.3(6)	108(28)
8889.8(12)	8889.8(12)	0	0 ⁺	82(16)	1	561(112)	1.2(3)	207(41)
9068.2(13)	9068.2(13)	0	0 ⁺	61(15)	1	432(103)	1.5(4)	150(36)
9273.9(15)	9273.9(15) ^g	0	0 ⁺	51(23)	1	380(168)	1.7(8)	124(55)
9300.4(15)	9300.4(15)	0	0 ⁺	111(45)	1	835(337)	0.8(3)	269(109)
9452.3(16)	9452.3(16)	0	0 ⁺	60(23)	1	465(176)	1.4(6)	143(54)
9466.8(35)	9466.8(35) ^g	0	0 ⁺	30(19)	1	232(149)	2.8(18)	71(46)
9830(4) ^k	9830(4)	0	0 ⁺	42(19)	1	354(162)	1.9(9)	97(44)

^aData taken from Ref. [44].

^bNot observed in $E_{e^-} = 6.0$ MeV measurement.

^cLevel strongly fed.

^dBranching ratio taken from Ref. [44].

^eSpin and parity taken from Ref. [44].

^fData from $E_{e^-} = 6.0$ MeV measurement.

^gHI γ S data indicates $M1/E1$ doublet.

^hDoublet with $9092.7 \rightarrow 2_1^+$.

ⁱEnergy and intensity from HI γ S data

^jDoublet with a single-escape peak.

^kLevel exclusively observed in HI γ S data.

TABLE IV. Nuclear data information observed for $J = 1$ levels in ^{60}Ni for which no parity information was obtained. Given are the level energy, E_R , and γ -ray energy, E_γ , of the depopulating transitions, the energy of the final level, E_f , spin and parity of the final level, J_f^π , the integrated cross section, $I_{S,f}$, the branching ratio, Γ_f/Γ , the ground-state width, Γ_0 , the level lifetime, τ , as calculated from Γ , and the reduced ground-state excitation probabilities, $B(\Pi 1, 0^+ \rightarrow 1^\pi)$.

E_R (keV)	E_γ (keV)	E_f^a (keV)	$J_f^\pi^a$	$I_{S,f}$ (eV b)	Γ_f/Γ	Γ_0 (meV)	τ (fs)	$B(\Pi 1, 0^+ \rightarrow 1^\pi)$ ($10^{-3} e^2(\text{fm})^2$) or ($10^{-3} \mu_N^2$)
3797.9(10)	3797.9(10)	0	0^+	3.1(4)	1	3.9(10)	170(22)	0.203(26)/18(3)
3908.1(3)	3908(3)	0	0^+	12.9(8)	1	17(1)	39(7)	0.82(15)/74(14)
5064.5(6) ^b	5065.4(7)	0	0^+	45.3(25)	0.81(2)	124(10)	4.30(41)	2.7(3)/247(18)
	3732.1(9)	1332.5	2_1^+	9.2(21)	0.19(3)			
5931.4(11) ^c	5930.8(11)	0	0^+	6.8(17)	1	21(5)	31(8)	0.285(70)/25.8(63)
6736.8(10) ^{d,e}	6736.1(16)	0	0^+	4.2(15)	0.46(11)	36(21)	8.4(49)	0.34(20)/31(18)
	4577.7(13)	2158.6	2^+	5.0(19)	0.54(11)			

^aData taken from Ref. [44].

^bIn Ref. [44] a negative parity is assigned tentatively.

^cContaminated by a ^{11}B transition.

^dSpin $J = (1)$ only tentatively assigned.

^eLevel seen only in $E_{e^-} = 8.0$ MeV measurement.

the experimental evidence indicates that they were fed, the 1984(2)-keV γ ray depopulating the third excited 0^+ level at 3318.6 keV also was observed. As it is in NRF experiments impossible to excite 0^+ levels directly, this represents an unambiguous evidence for strong feeding. Because the photon flux in the energy region between 8.0 and 9.9 MeV is low the branching states are rather weakly excited. Furthermore, the transitions connecting these weakly excited levels with lower-lying excited states are found in an energy range where in spectra recorded with bremsstrahlung in the entrance

channel the nonresonant background is already considerable. Therefore, only a few of these transitions could be resolved, an observation that is in accordance with results extracted from the HI $\vec{\gamma}$ S measurements previously published [50]. In the HI $\vec{\gamma}$ S spectra measured with the setup of four HPGe detectors in a crosslike geometry, in addition to the γ -ray transitions depopulating the photoexcited $J = 1$ levels to the ground-state transitions depopulating low-lying excited states also were observed. Because the latter cannot be excited with the quasimonochromatic photon beam directly from the

TABLE V. Nuclear data information observed for $J^\pi = 2^+$ levels in ^{60}Ni . Given are the level energy, E_R , and γ -ray energy, E_γ , of the depopulating transitions, the energy of the final level, E_f , spin and parity of the final level J_f^π , the integrated cross section, $I_{S,f}$, the branching ratio, Γ_f/Γ , the ground-state width, Γ_0 , the level lifetime, τ , as calculated from Γ , and the reduced ground-state excitation probabilities, $B(E2, 0^+ \rightarrow 2^+)$. In cases, where feeding from higher-lying states is evident, only limits are given.

E_R (keV)	E_γ (keV)	E_f^a (keV)	$J_f^\pi^a$	$I_{S,f}$ (eV b)	Γ_f/Γ	Γ_0 (meV)	τ (fs)	$B(E2, 0^+ \rightarrow 2^+)$ ($e^2(\text{fm})^4$)
1332.7(2) ^b	1332.7(2)	0	0^+	<8.6(8)	1	<1.32(4)	>500(17)	<1950(60)
2157.7(10) ^c	2157.7(10)	0	0^+	<6.4(17)	0.15(2) ^d	<10(4)	>9.6(48)	<1370(520)
3123.4(8) ^c	3123.3 ^e	0	0^+		0.09(1) ^d	<11(8)	>5.2(41)	<239(171)
	1790.9(9)	1332.5	2_1^+	<19.4(4.3)	0.86(4) ^d			
3268.9(11) ^c	3268.9 ^e	0	0^+	<7.4(27)	0.15(1) ^d	<9(2)	>10.7(3)	<157(53)
	1936.4(11)	1332.5	2_1^+		0.43(2) ^d			
3392.3(10) ^c	3392.3 ^e	0	0^+	<14.5(37)	0.06(2) ^d	<10(14)	>3.5(6.0)	<144(193)
	2059.8(10)	1332.5	2_1^+		0.84(6) ^d			
4006.7(8) ^b	4006.7(1.1)	0	0^+	4.2(4)	0.38(2) ^d	7.8(15)	31.7(58)	47(7)
4844.5(7) ^b	4844.5(7)	0	0^+	6.1(8)	0.33(2) ^d	22.6(71)	10(3)	52(12)
6229.0(11) ^f	6229.0(11)	0	0^+	11.4(24)	1	23(5)	28.7(60)	15(3)

^aData taken from Ref. [44].

^bData from $E_{e^-} = 6.0$ MeV measurement.

^cOnly seen in $E_{e^-} = 10.0$ MeV measurement.

^dBranching ratio taken from Ref. [44].

^eTransition not observed.

^fSpin $J = (2^+)$ tentatively assigned.

ground state the population of these levels stems from inelastic decays of the photoexcited $J = 1$ states. Only a few peaks corresponding to these inelastic transitions connecting the spin-1 levels and the lower-lying levels were resolved from the background.

A. Additional results for ^{58}Ni

Because the two complementary ($\vec{\gamma}$, γ') measurements exploiting the clover and two-HPGe-detector setup employed a Ni target of natural composition, in these measurements additional spectroscopic information about the parity of $J = 1$ states in ^{58}Ni was obtained. The latter has a natural abundance of 68.1% (^{60}Ni : 26.2%). For 13 spin-1 states parities assigned in a NRF experiment with partially polarized bremsstrahlung

TABLE VI. A comparison of parity assignments for levels of ^{58}Ni obtained in the ($\vec{\gamma}$, γ') reaction with quasimonochromatic photons at the H $\vec{\gamma}$ GS facility using a natural Ni sample with previously published results [38] obtained using partially polarized bremsstrahlung in the entrance channel. For the energies, the literature values [38] are used.

Energy ^a	J_{Lit}^{π}	J^{π}	Comment
9368.5	1 ⁽⁻⁾	1 ⁻	
9326.4	1	1 ⁺	
9190.7	1 ⁻	1 ⁻	
9156.9	1 ⁺	1 ⁺	
9073.4	1 ⁺	1 ⁺	
8961.3	1	1 ⁺	
8934.6	1	1 ⁻	
8880.2	1 ⁻	1 ⁻	
8857.4	1	1 ⁺	Additional branch at 7402 keV.
8679.3	1 ⁺	1 ⁺	
8600.5	1 ⁺	1 ⁺	
8552.7	(1)		Not present in spectrum
8514.1	1 ⁻	1 ⁻	
8461.0	1 ⁺	1 ⁺	
8395.1	1 ⁻	1 ⁻	
8317.1	1	1 ⁻	
8237.3	1 ⁻	1 ⁻	Additional branch at 6785 keV
8096.3	1		Not present in spectrum 9554.0 keV \rightarrow 1457 keV
8068.6	(1) ⁽⁻⁾	1 ⁻	
7876.7	1	1 ⁺	
7766.0	(1)	(1) ⁺	
7709.7	1 ⁺	1 ⁺	
7388.8	1 ⁺	1 ⁺	
7271.7	1	1 ⁻	
7249.6	(1)	1 ⁻	
7048.2	1 ⁻	1 ⁻	
6892.9	(1)	1 ⁻	
6685.0	1	1 ⁺	
6430.7	1		Not present in spectrum 7876.7 keV \rightarrow 1457 keV
6424.9	1		Not present in spectrum 9630.5 keV \rightarrow 2902 keV
6027.3	1	1 ⁻	
5905.3	1 ⁺	1 ⁺	

^aData taken from Ref. [38].

in the entrance channel [38] could be confirmed and for 14 levels the parity was assigned for the first time. The results are presented in Table VI. Additionally, for transitions that from the published level scheme were expected to be present in the spectra but were not seen, new possible placements in the level scheme are proposed. Therefore, the Ritz variation principle was applied until the addition of the γ -ray energy and the excitation energy of a low-lying level resulted in the energy of a higher-lying spin-1 state.

IV. DISCUSSION

The parity information obtained in the HI $\vec{\gamma}$ S experiment in combination with the data obtained in the DHIPS experiment allows for a determination of the photoresponse of ^{60}Ni . These experimental results can be used to test calculations within the QPM. Furthermore, a comparison with ^{56}Fe [38,39] and ^{58}Ni [38], whose data set was improved with the HI $\vec{\gamma}$ S campaign, allows for an investigation of the evolution of the PDR in these $f p$ -shell nuclei with only a small neutron excess.

To be able to draw a final picture, for the spin-1 levels with undetermined parity the assumption is made that below the candidate for the $[2_1^+ \otimes 3_1^-]_1$ - quadrupole-octupole coupled state all $J = 1$ levels are of positive parity and above this particular 1⁻ level a negative parity is assumed. Because in ^{60}Ni , as well as in ^{58}Ni , for the vast majority of levels a firm parity assignment was made the general picture is affected only to a minor extent.

In this work for a better comparability between $M1$ - and $E1$ -excited levels the reduced ground-state transition widths, $\Gamma_0^{\text{red}} = \Gamma_0/E_\gamma^3$, are plotted. To obtain a more global picture the strengths of the individual $J = 1$ levels were artificially broadened with a Breit-Wigner curve,

$$\Gamma_0^{\text{red}}(BW, E) = \frac{C}{2\pi} \sum_i \frac{\Gamma_{0,i}^{\text{red}}(\text{exp})}{(E - E_i)^2 + \frac{\Delta^2}{4}}. \quad (8)$$

For a given parity the broadened curves were added up to display a resonancelike structure. If not indicated to be different, a width of $\Delta = 200$ keV was used. This width was chosen as a compromise that makes it possible to highlight the global structure but fine details are still visible. Using a constant factor, $C = 250$, the maximum height of the curves was adjusted to the data for the discrete levels. For the QPM curves the same factors, $C = 250$, were used as for the corresponding experimental curves but for the clarity of the presentation had to be downscaled by additional factors which are indicated. In all experimental plots above 9.5 MeV a decrease of this summed curve is visible. This decrease is, of course, caused by the fact that no higher-lying levels were observed and, therefore, their strength is missing at the upper end.

For the calculations within the QPM framework, first the single-particle basis was calculated using the Woods-Saxon potential as the mean field. The results are checked as to whether they reproduce the experimentally observed low-lying levels of the adjacent odd-mass nuclei. Interestingly, on this mean-field plus pairing stage the $E1$ strength is carried by two-quasiparticle excitations. In the framework of the shell model these particular two-quasiparticle excitations can be associated

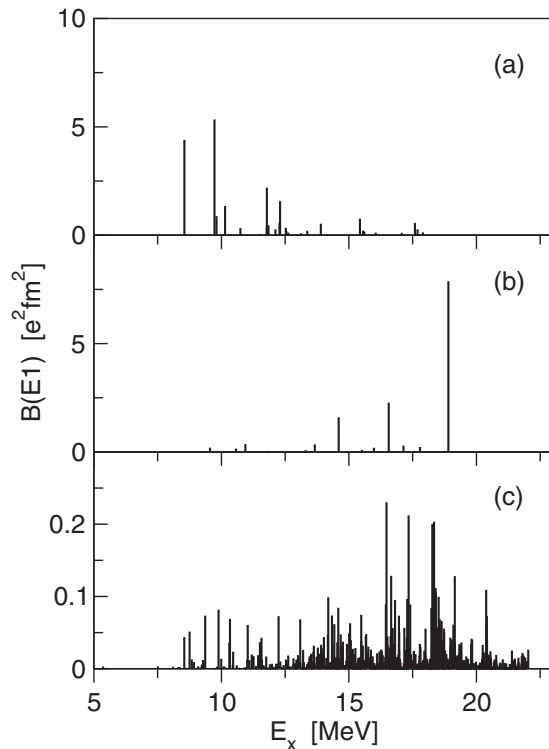


FIG. 5. Evolution of the $B(E1)$ -strength distribution of ^{60}Ni in the different steps of the QPM. On the mean-field + pairing level the $E1$ strength is contained in one-particle, one-hole (two-quasiparticle) excitations (a). Applying the residual, repulsive dipole-dipole interaction in the stage of the quasiparticle random phase approximation formalism (b) deploys a vast fraction of the $E1$ strength into the region of the GDR. On the QPM level (c) the fragmentation is reproduced by considering the interaction with other complex configurations. In part (c) 1^- states up to the second phonon order are considered. Figure 6(a) shows the fragmentation when the model space includes three-phonon configurations. A more detailed discussion is given in the text. Note the different scales on the y axis.

with one-particle, one-hole (1p1h) excitations across a major shell gap such as $[0d_{3/2^+}, 1p_{1/2^-}]_{1^-}$ or $[0f_{7/2^-}, 0g_{9/2^+}]_{1^-}$. Configurations containing four or more quasiparticle excitations do not carry any substantial $E1$ -excitation strength. The corresponding $E1$ -strength distribution is shown in Fig. 5(a). For the $J^\pi = 1^+$ levels the major components carrying most of the $M1$ strength are the spin-flip configurations, such as $[1p_{3/2^+}, 1p_{1/2^+}]_{1^+}$ and, in particular, $[0f_{7/2^+}, 0f_{5/2^+}]_{1^+}$.

The next step demands solving the secular equations of the quasiparticle random phase approximation (QRPA) using separable residual multipole-multipole forces. The corresponding residual strength parameters are adjusted to reproduce the properties of the lowest 2_1^+ and 3_1^- excited states. This procedure provides a basis of QRPA phonons, which in this work includes QRPA phonons with angular momentum ranging from $J^\pi = 0^\pm$ to $J^\pi = 8^\pm$. In addition to several collective phonons, 2_1^+ , 2_{ms}^+ , or 3_1^- or the ones representing giant resonances, the QRPA equations yield many almost pure two-quasiparticle excitations. Here, the latter are also referred to as phonons and are included in the basis. Phonons of a given multipolarity

but different microscopic structure are distinguished by the so-called root-order quantum number, i . By collectivity we mean the situation when many 1p1h (or two quasiparticle) components give substantial contribution to the phonon's wave function leading to enhanced $B(E\lambda)$ values of their excitation. The most collective phonon is the lowest 1^- phonon. This phonon represents the spurious state corresponding to a translation of the entire nucleus. Its energy is set to zero by adjusting the isoscalar residual strength parameter. Later it is excluded from the phonon basis. Owing to the repulsive nature of the isovector dipole-dipole residual interaction the initial 1p1h excitations [Fig. 5(a)] deplete their $E1$ strength to higher-lying 1^- phonons [see Fig. 5(b)]. Thus, the $E1$ strength below the GDR is just the debris of these 1p1h excitations.

For the magnetic excitation it is the spin-isospin residual force that mixes the 1p1h spin-flip excitations into an isoscalar and isovector combination.

In the next step, essentially the QPM approach, the physically observed states are obtained by a final diagonalization of the Hamiltonian. In the model used in this work couplings up to the third phonon order were considered. Furthermore, quasiparticle excitations with higher numbers of quasiparticles, such as four and six quasiparticles, are considered. The two-quasiparticle (or one-phonon) excitations couple to four-quasiparticle (or two-phonon) excitations; the four-quasiparticle configurations interact with six-quasiparticle (or three-phonon) configurations. The latter results in a (quasi-) continuum of 1^- levels forming the GDR. Despite generating the $B(E1)$ strength of the GDR, the 1p1h excitations contribute less than 1% to the wave function of each particular state in the GDR energy region.

The increase of the fragmentation with inclusion of higher phonon orders is obvious when comparing the $B(E1)$ -strength distribution in Fig. 5(b) obtained within the QRPA to the ones in Fig. 5(c) with configurations up to the second phonon order and in Fig. 6(b) including three-phonon configurations. Previous comparisons (e.g., see Ref. [12]) have shown the latter to be sufficient to reproduce the observed degree of fragmentation. The same holds true for the fragmented $M1$ strength of the $M1$ resonances.

Considering the above-mentioned picture, it is natural to expect a dependence of the energy region in which the PDR strength is located from the evolution of the subshells in a specific mass region. The information about the latter can be obtained from particle-transfer experiments. A detailed study of the evolution of subshells within the fp shell and for the $0g_{9/2^+}$ has been performed exploiting neutron-adding, neutron-removing, and proton-adding reactions [51]. The results of these studies are in good agreement with particle-transfer experiments evaluated in the NNDC database [44]. The latter provides additional information on the orbitals of the sd shell.

For the $J^\pi = 1^-$ levels discussed in this work, the energy difference between two subshells originating from a different oscillator shell, and therefore having different parity, is important. Recently, in Ref. [51] it has been demonstrated that the energy gap between the neutron $0f_{7/2^-}$ and $0g_{9/2^+}$ subshells shrinks towards the heavier, stable nickel isotopes, while for the protons this energy gap remains rather constant.

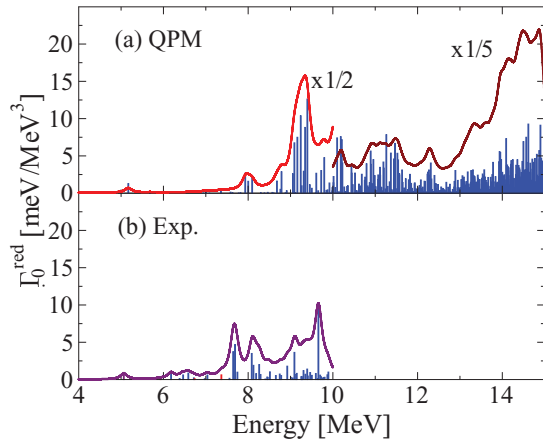


FIG. 6. (Color online) Distribution of $E1$ -excitation strength as obtained from QPM calculations (a) and the DHIPS measurements (b). Levels with a firmly assigned $J^\pi = 1^-$ are plotted as blue bars and $J = 1$ levels for which no parity information is known as red bars. Plotted is the reduced ground-state transition width, $\Gamma_0^{\text{red}} = \Gamma_0/E_\gamma^3$, as a function of the level excitation energy, E_R . The corresponding $B(E1, 0^+ \rightarrow 1^-)$ excitation strength calculates to $B(E1, 0^+ \rightarrow 1^-)[10^{-3} e^2(\text{fm})^2] = 2.865\Gamma_0^{\text{red}}[\text{meV}/\text{MeV}^3]$. The solid lines represent the sums of all levels excitation strength broadened with a Breit-Wigner curve of 200 keV width.

The energy gap between the proton fp and sd shells is smaller ($\Delta E \approx 3\text{--}5$ MeV) than for the corresponding neutron orbitals ($\Delta E \approx 6$ MeV) [44]. This simple approach allows for the conclusion that the onset of the PDR $E1$ strength can be expected to be lower in ^{60}Ni than in ^{58}Ni .

In closed-shell nuclei the single-particle structure of stronger excited positive-parity $J = 1$ states is dominated by $[nl_{j-1/2}, nl_{j+1/2}]$ spin-flip excitations. The particle-transfer experiments [44,51] demonstrate that in the Ni isotopes the energy difference of the corresponding $1p_{1/2^-}$, $1p_{3/2^-}$, and $0f_{5/2^+}$, $0f_{7/2^+}$ spin-orbit partner orbitals remains, apart from small shifts owing to a slight change in the occupancy numbers of the orbitals, constant. Considering the spherical nature of the nuclei situated on or near the $Z = 28$ shell closure, it is reasonable to assume an identical potential well. Hence, the spin-orbit splitting can be expected to be similar.

For ^{58}Ni [38], as well as for ^{60}Ni [50], evidence for strong branchings other than the ground-state decay of the photoexcited spin-1 levels was observed. For ^{58}Ni the energy range in which these levels are located could be determined only to be within 6 and 10 MeV, the end-point energies of the measurements. In this work a more detailed picture was obtained for ^{60}Ni . In the $\text{HI}\bar{\gamma}\text{S}$ measurements some transitions were firmly identified as inelastic, and even more were identified as such in the DHIPS measurements. However, both parts of the campaign showed substantial evidence that there is a vast number of weaker unidentified branches from the photoexcited spin-1 states to lower-lying excited states.

As demonstrated in Fig. 4 in the DHIPS measurement the angular distributions of the low-lying levels provided evidence for strong feeding. Further evidence is provided by the observation of the 1986-keV γ ray in the 9.9-MeV DHIPS measurement. This γ -ray transition depopulates the

TABLE VII. Average ground-state branchings ratios (Γ_0/Γ) in percent as determined exploiting quasimonoenergetic photon beams at $\text{HI}\bar{\gamma}\text{S}$. Presented are the values considering all excited $J = 1$ states (a) [50], only the negative-parity (b), and only the positive-parity (c) spin-1 levels for the respective beam energy (in units of MeV).

E_{beam} :	7.65	8.12	8.46	8.76	9.11	9.31	9.66
(a)	80(7)	74(6)	56(8)	49(8)	59(7)	54(7)	56(7)
(b)	78(8)	71(7)	49(9)	36(7)	50(7)	40(7)	55(7)
(c)	34(13)	32(8)	24(7)	28(7)	31(7)	31(6)	3(2)

0_3^+ level at 3318 keV. Because a 0^+ level cannot be excited by a real photon, the only way the level can be populated is by feeding from higher-lying levels. The exploitation of quasimonoenergetic photon beams in the entrance channel made it possible to obtain a more detailed picture. In the $\text{HI}\bar{\gamma}\text{S}$ measurement the observed depopulation of lower-lying excited levels allowed for the determination of average branching ratios for the energy regions ($\Delta E \approx 300$ keV) covered by the incident photon beam (see Fig. 4 in Ref. [50]). For completeness, the results of this analysis are presented in Table VII and extended with respect to a given parity of the excited spin-1 levels. In this table the ground-state branching ratios are given considering all observed spin-1 states (a), only the negative-parity states (b), and the positive-parity levels (c). At the current level of experimental sensitivity it is impossible to attribute the observed population of lower-lying levels as branching to any specific $J = 1$ states.

In ^{62}Ni it was possible to observe the decay behavior for one individual 1^- level at 7646 keV [53]. Here, a random overlap of γ rays produced in the $^{56}\text{Fe}(n, \gamma)$ reaction and the 7646-keV level was used to populate this level. The low number of photons in the entrance channel concentrated in a narrow energy range resulted in a comparably low background owing to atomic scattered photons and, therefore, in an enhanced sensitivity of this experiment. In total, 12 decay branches originating from this level were observed. The ground-state branching ratio of this level was determined to $\Gamma_0/\Gamma = 0.64$. This is even more remarkable as the level itself has a $B(E1, 0^+ \rightarrow 1^-)$ strength of only $1.97(10) \times 10^{-3} e^2(\text{fm})^2$, rather moderate. Many of the weak branches observed in this level of ^{62}Ni are in a NRF experiment using bremsstrahlung in the entrance channel below the sensitivity limit. The attribution of further decay channels ($\Gamma_0/\Gamma < 1$) to a given level increases its ground-state decay width Γ_0 [see Eq. (3)]. Consequently, the $B(\Pi 1, 0^+ \rightarrow 1^\pi)$ excitation probability increases as well. Owing to the inability to resolve many of the observed decays to low-lying levels in many cases the excitation strength of the observed $J = 1$ levels is certainly underestimated. Hence, the strength distributions might be subject to change, when future experiments are capable of overcoming the present drawbacks discussed above. Nevertheless, in the following the picture is discussed that is drawn by the present measurement when the identified branches are included. However, because in NRF experiments the integrated cross section, $I_{S,0}$, depends only on experimental quantities, it is fully determined. Consequently, if future experiments provide additional information about the full sets of branches of individual levels, the integrated cross

sections of the ground-state branch, $I_{S,0}$, presented in Tables II, III, IV, and V allow for a calculation of the revised quantities.

The additional parity information of spin-1 levels in ^{58}Ni allows for a comparison with ^{60}Ni . Hence, it is possible to draw conclusions about the evolution of the dipole strength in these almost $N = Z$, fp -shell nuclei. Further detailed spectroscopic information about the dipole strength in this mass region is available for ^{56}Fe . However, it has to be mentioned that all the (γ, γ') measurements from which these data sets have been obtained suffer from their limited end-point energy. For all isotopes under consideration the neutron separation energy is higher than the maximum photon energies used ($E_\gamma \leq 10$ MeV). In the case of ^{60}Ni this threshold was determined by the maximum electron energy of 10 MeV that the injector part of the S-DALINAC can provide. The experiments for ^{56}Fe and ^{58}Ni were performed with the same end-point energies. Therefore, only the different sensitivities achieved with the different setups are of importance when comparing the data sets. The latter was improved for ^{60}Ni , because the spectra recorded with quasimonoenergetic beams at HI γ S have, owing to the absence of escaped Compton-scattered events, a strongly improved peak-to-background ratio in the energy range covered by the incident photon beam. This enhanced sensitivity enabled the observation of weaker excited levels especially near the end-point energy of the bremsstrahlung measurements.

A. $E1$ -strength distribution for ^{60}Ni

Using the combined data of the bremsstrahlung and polarized photon beams a detailed picture of the $E1$ -excited levels up to 10 MeV can be drawn. The experimental results will be compared to QPM calculations. The corresponding strength distributions are illustrated in Fig. 6. It is obvious that, compared to the experimental strength distribution [Fig. 6(b)], the theoretical strength distribution [Fig. 6(a)] is slightly shifted to higher energies. In the experiment an accumulation of stronger excited levels is visible in the range between 7.5 and 8.2 MeV.

The lowest-lying candidate for a $J^\pi = 1^-$ level in ^{60}Ni is observed at 5064 keV. However, in this work it was not possible to firmly assign a parity to this level. In previous work, this level was assigned as the 1^- member of the $[2_1^+ \otimes 3_1^-]_{1-}$ quadrupole-octupole coupled (QOC) two-phonon quintuplet [19,52]. Its excitation energy is slightly lower than the sum energy (5372 keV) of the 2_1^+ quadrupole ($E_{2_1^+} = 1332$ keV) and 3_1^- octupole phonon ($E_{3_1^-} = 4040$ keV). In this work it was possible to firmly assign a negative parity to the candidate for the corresponding state in ^{58}Ni . This level at 6030 keV is found at a higher energy compared to the corresponding state in ^{60}Ni . This change in excitation energy is easily understood on a microscopic level. In this particular mass region the major contributions to the octupole phonon are given by the $\Delta l = 3$, $\Delta j = 3$: $[p_{3/2^-}, g_{9/2^+}]_{3-}$ subshell combinations, which, considering the above-mentioned shell structure, require less excitation energy for ^{60}Ni . For ^{58}Ni the sum energy (5929 keV) of the two contributing phonons ($E_{2_1^+} = 1454$ keV; $E_{3_1^-} = 4475$ keV) is less than the experimentally observed energy of the QOC 1^- level ($E_{[2_1^+ \otimes 3_1^-]_{1-}} = 6030$ keV). Again, this anharmonicity can easily be understood from a microscopic

point of view. ^{58}Ni can be considered as two neutrons coupled to the doubly magic ^{56}Ni core. When producing the particle-hole excitation necessary to create the octupole phonon, the neutron is no longer available to contribute to the seniority-two-dominated quadrupole excitation and vice versa. Nevertheless, the observed branching behavior for the QOC states in ^{58}Ni and ^{60}Ni is quite similar. The ground-state branching ratio is $\Gamma_0/\Gamma = 0.81$ for either nucleus.

The evolution of $B(E1)$ strength of this QOC levels in the two adjacent even-even Ni isotopes is somewhat puzzling. The 6030-keV level in ^{58}Ni [$B(E1) \uparrow = 5.69(16) \times 10^{-3} e^2(\text{fm})^2$] is, in comparison to the 5064-keV level [$B(E1) \uparrow = 2.7(3) \times 10^{-3} e^2(\text{fm})^2$] in ^{60}Ni , more than twice as strongly excited. There could be two reasons for this. The first could be an experimental one. In the 6.0-MeV measurement of ^{60}Ni a γ ray at 1357.2(3) keV was observed. Its energy does not correspond to a known background line or a transition in the boron calibration standard. For ^{60}Ni the only possible placement for this γ ray in the low-energy level scheme is between the 5064-keV level and a possible level at 3709 keV. With the inclusion of this γ ray in the decay scheme of the 5064-keV level its $B(E1) \uparrow$ strength is calculated to be $7.1(8) \times 10^{-3} e^2(\text{fm})^2$, a value comparable to the $B(E1) \uparrow$ strength for the QOC two-phonon 1^- state in ^{58}Ni . Indeed, at 3709 keV a peak was observed. However, at this energy a line stemming from a neutron-capture reaction is commonly observed in spectra recorded at the DHIPS setup. Because the samples are contained in polyethylene containers and the detectors are surrounded with massive lead shielding, the production of neutrons in the $^{13}\text{C}(\gamma, n)$ (^{13}C : $E_n = 4946$ keV) and $^{207}\text{Pb}(\gamma, n)$ (^{207}Pb : $E_n = 6738$ keV) reactions is unavoidable. However, the intensity of the 3709-keV peak is not sufficient, as expected, if the possible level at 3709 keV were fed from the 5064-keV level via this 1357-keV γ ray. In a previously published (n, γ) measurement [54] a γ ray at 1358 keV was observed, but no γ ray at 3709 keV was reported. Following these considerations, the 1357-keV γ ray was not assigned to the 5064-keV level. It remains unplaced in the level scheme. Consequently, at present an explanation for the strongly deviating $B(E1)$ strength based on the structure of the QOC states in the two Ni isotopes is more likely. As outlined in Refs. [19] and [55], the QOC 1^- level strongly interacts with the GDR and very likely also with states forming the PDR. For semimagic nuclei this interference is constructive and becomes enhanced when approaching a doubly magic nucleus. The QPM calculations reproduce nicely the observed drop in strength. For ^{58}Ni a strength of $B(E1) \uparrow = 6 \times 10^{-3} e^2(\text{fm})^2$ and for ^{60}Ni a strength of $B(E1) \uparrow = 3.7 \times 10^{-3} e^2(\text{fm})^2$ is calculated.

The levels between 6180 and 7040 keV are situated close to the sum energy of the 2_2^+ and 4_1^+ states and the 3_1^- octupole phonon. In ^{62}Ni it has been shown [56], that the vibrational picture holds for the $[2^+ \otimes 2^+]_J$ ($J = 0^+, 2^+, 4^+$) two-phonon triplet. Therefore, it is reasonable to assume that the 2_2^+ and 4_1^+ states in ^{60}Ni are also members of this two-phonon triplet. The energy qualifies in particular the 6180-keV level as a candidate for a $[[2_1^+ \otimes 2_1^+]_{2_2^+} \otimes 3_1^-]_{1-}$ level [$E(2_2^+) + E(3_1^-) = 6194$ keV]. The summed energy of the 4_1^+ level and the octupole phonon is 6544 keV. In ^{58}Ni the

corresponding sum energies are $E(4_1^+) + E(3_1^-) = 6933$ and $E(2_2^+) + E(3_1^-) = 7250$ keV. Indeed, at 7048 and 7271 keV two stronger excited 1^- levels are observed. Further strong arguments for these levels of ^{60}Ni to have at least a considerable three-phonon component in their wave functions are the observed decay branchings to the one- and two-phonon states. For the candidates in ^{58}Ni no such decays were observed. Theoretically, the $E1$ decay is described by a one-body external field. However, the three-phonon annihilating transition to the ground state indicates admixtures of other configurations, such as the $E1$ strength generating two-quasiparticle excitations.

Above 7.5 MeV a vast number of $J^\pi = 1^-$ levels is observed. The nature of these levels has been discussed in a previous publication [50]. Within this work the indirectly observed branching ratios to lower-lying levels were used to demonstrate the crossover from 1p1h-dominated 1^- levels around 8 MeV to levels whose wave functions contain more complex structures. Indeed, for the levels situated between 7.5 and 8.3 MeV only a moderate average branching ratio of $\approx 20\%$ to the 2_1^+ , 2_2^+ , and 0_2^+ levels was observed. For the levels above 8.4 MeV the observed mean branching ratio extended even more than 40% and the number of final states increased drastically. In the latter study, the branching ratios were calculated including all dipole excited states. Under the assumption that none of this branching stems from a $J^\pi = 1^+$ level, the observed ground-state branching ratios drop even further, which leads to an additional amount of $E1$ strength. The corresponding ground-state branching ratios Γ_0/Γ are presented in Table VII.

In the DHIPS measurement at least for the strongly excited levels a branching should have been observed but this was the case for only a few levels. For example, the comparably strongly excited levels at 8923, 9093, and 9659 keV exhibit only moderate branchings to the first excited 2_1^+ level. The observed branchings of these strongly excited levels are always below the average values obtained in Ref. [50]. In addition to the enhanced ground-state transition strength, this observation indicates that these levels have a stronger 1p1h component in their wave functions as well. Therefore, it can be concluded that the vast majority of the observed branching stems from seemingly weakly excited levels. Consequently, a measurement in which these branches could be observed would raise the $B(E1) \uparrow$ strength of these levels. Furthermore, the measurement suffers from a limited experimental sensitivity caused by the background and low photon flux near the end-point energy. Hence, the comparison of the experimental $B(E1) \uparrow$ strength obtained in the bremsstrahlung measurement and the theoretical strength from the QPM calculations is somewhat questionable. Nevertheless, summing the $B(E1) \uparrow$ strength observed in the DHIPS measurement in the energy region above the QOC level results in a total $B(E1) \uparrow = (153.8 \pm 9.5) \times 10^{-3} e^2(\text{fm})^2$. That value corresponds to 0.5% of the TRK sum rule [1]. Including only the levels up to 10 MeV, the theoretical value of the QPM is $B(E1) \uparrow = 237.8 \times 10^{-3} e^2(\text{fm})^2$. For the comparison it has to be considered that the calculations result in a $\langle 1^- || \hat{E}1 || 0^+ \rangle$ matrix element. That means the excitation strength is calculated straightforwardly and does not depend on possible branches to lower-lying states. The

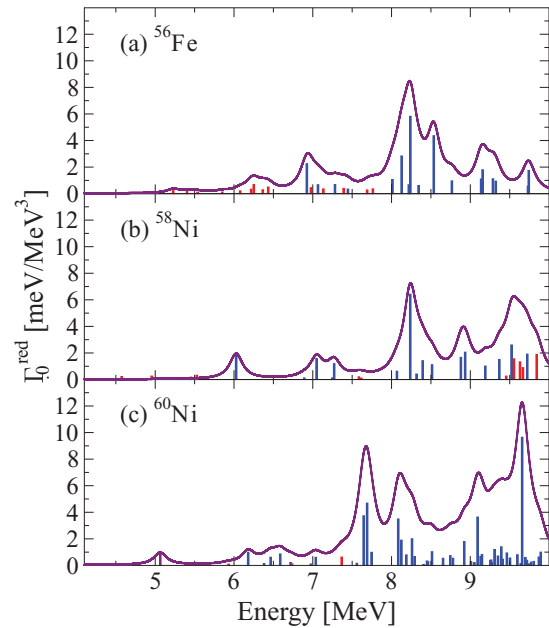


FIG. 7. (Color online) Distribution of $E1$ -excitation strength as measured for (a) ^{56}Fe [38,39], (b) ^{58}Ni [38], and (c) ^{60}Ni . Levels with a firmly assigned $J^\pi = 1^-$ are plotted as blue bars and $J = 1$ levels for which no parity information is known as red bars. Plotted is the reduced ground-state transition width, $\Gamma_0^{\text{red}} = \Gamma_0/E_\gamma^3$, as a function of the level excitation energy, E_R . The corresponding $B(E1, 0^+ \rightarrow 1^-)$ excitation strength calculates to $B(E1, 0^+ \rightarrow 1^-)[10^{-3} e^2(\text{fm})^2] = 2.865\Gamma_0^{\text{red}}[\text{meV}/\text{MeV}^3]$. The solid line represents the sum of all levels' excitation strength folded with a Breit-Wigner curve of 200 keV width.

discrepancy between experiment and theory can be resolved when including the branching ratios determined in the HI γ S campaign. Using the measured $\Gamma_0^{\text{red}}/\Gamma$ value of each individual level and applying it to those of the branching ratio as given in part (b) of Table VII, the summed $B(E1) \uparrow$ strength raises to $[250.9 \pm (15.7_{\text{stat}} + 15.4_{\text{sys}})] \times 10^{-3} e^2(\text{fm})^2$. This value exhausts 0.8% of the TRK sum rule. This value drops to $[225.0 \pm (14.6_{\text{stat}} + 14.3_{\text{sys}})] \times 10^{-3} e^2(\text{fm})^2$ when the $J^\pi = 1^+$ levels are included in the ground-state branching ratios [part (a) of Table VII]. The systematic error stems from the attribution of levels seen in two HI γ S measurements with different mean photon energies for them both and, therefore, having a different mean branching ratio. However, as shown in Fig. 6(a) the theoretical $E1$ -strength distribution starts at too high energies when compared to the experimental one [Fig. 6(b)]. By optical comparison the theoretical distribution is shifted by ≈ 1.5 MeV to higher energies. Considering this shift and summing the theoretical strength up to an energy of 11.5 MeV results in a total $B(E1) \uparrow = 647 \times 10^{-3} e^2(\text{fm})^2$, a value certainly too high when compared to the experimental $E1$ strength.

In Fig. 7 the $E1$ -strength distributions of ^{56}Fe [Fig. 7(a)] [38,39], ^{58}Ni [Fig. 7(b)] [38], and ^{60}Ni [Fig. 7(c)] are shown. The three strength distributions exhibit a similar pattern. In particular, the stronger excited levels near 8 MeV excitation energy are obvious. Especially the two Ni isotopes exhibit, apart from a ≈ 700 -keV shift of the two strength distributions, a

strong resemblance. This resemblance becomes even stronger when considering results from other experimental approaches. In $^{58}\text{Ni}(p, p')$ [22] and $^{58}\text{Ni}(e, e')$ [57] experiments, a strongly excited spin-1 level at 10.67 MeV was observed. Assuming this level to have a negative parity, the two Ni isotopes exhibit an identical four-hump structure in the folded curve. Concerning the parity assignments in the (e, e') experiment it was already pointed out in Ref. [38] that in this experiment several parities were assigned wrongly, e.g., the parities of the 8237-, 8514-, 8880-, 9369-, and 9523-keV levels. This is somewhat puzzling because these levels are the five strongest excited ones. A comparison of the excitation probabilities obtained with NRF and inelastic electron scattering resulted, except for the 8880-keV level, in a good agreement of the two experimental methods. For the 8880-keV level, the excitation strength obtained in the (e, e') experiment exceeds the value obtained in NRF by a factor of 3, indicating strong unobserved branchings from this particular level. Assuming a negative parity, the strongly excited 10.67-MeV level can be associated with the strongly excited level at 9.659 MeV in ^{60}Ni . In this case for the folded curve an almost identical four-hump structure is noticeable. Essentially, the only two differences are the shift of ≈ 700 keV to lower energies in ^{60}Ni and the increased degree of fragmentation for this nucleus. The decrease in excitation energy can be explained with the previously mentioned closure of the energy gap between the neutron $0f_{7/2+}$ and $0g_{9/2+}$ subshells in the more neutron-rich isotopes. Using the spectroscopic-factor-weighted values as published in Ref. [51], the energy gap between these particular subshells calculates to 5.7 MeV for ^{58}Ni and 5.1 MeV for ^{60}Ni . Estimating the pairing energy from the occurrence of the first noncollective states to be between 2.5 and 3 MeV, the sum of the energy for the subshell gap and the pairing is close to 7.5 and 8 MeV. This corresponds to the excitation energy where in the two Ni isotopes discussed here stronger excited 1^- levels are observed. The energy gap for the corresponding proton subshells calculates to 4.4 MeV for ^{58}Ni and 4.0 MeV for ^{60}Ni . This qualifies the levels between 6.5 and 7.0 MeV, previously ascribed to have a three-phonon character as the debris of the corresponding proton $1p_{1h}$ excitation.

The similarity of the two Ni isotopes is also reflected in the observed $B(E1)$ strengths. If for ^{60}Ni the 700-keV shift to lower energies is considered, the summed $B(E1)$ strength in the energy range between 6 and 9.3 MeV is $(100.4 \pm 4.2) \times 10^{-3} e^2(\text{fm})^2$. For ^{58}Ni , in the energy range above 6.1 MeV an accumulated $B(E1)$ strength of $(86.4 \pm 1.4) \times 10^{-3} e^2(\text{fm})^2$ was determined. Values that are in good agreement when considering the slightly improved sensitivity for the ^{60}Ni experiment and the uncertainty owing to the unseen branching transitions. For ^{56}Fe a total $B(E1)$ strength of $\sum B(E1) \uparrow = (79.6 \pm 1.5) \times 10^{-3} e^2(\text{fm})^2$ was obtained in the energy range from 6.9 to 9.8 MeV [39]. Despite the excellent work done in Ref. [39], there are still several spin-1 levels for which no parity is assigned. Assuming that the candidate for the $[2_1^+ \otimes 3_1^-]_1^-$ two-phonon excitation at 5228 keV [19] and all levels above have a negative parity an additional $E1$ strength of $(13.1 \pm 0.9) \times 10^{-3} e^2(\text{fm})^2$ can be added and the total $E1$ strength in ^{56}Fe below 10 MeV rises to $(92.7 \pm 1.7) \times 10^{-3} e^2(\text{fm})^2$.

However, because the experimental approach chosen in this work does not allow for the observation of levels with an excitation energy higher than the 9.9-MeV end-point energy, it is not even possible to determine the entire $E1$ strength below the neutron separation threshold. Therefore, no final conclusion about the amount of $E1$ strength attributed to the PDR can be made. Hence, a comparison to ^{68}Ni [20] for which the $E1$ strength was found near 11.5 MeV is rather pointless.

Apart from the branching behavior discussed in Ref. [50] the experimental finding that in ^{60}Ni , in comparison to ^{58}Ni , the $1p_{1h}$ -dominated 1^- levels are found at lower energy indicates the dependency of the $E1$ strength of the underlying shell structure. The shell structure has been highlighted before, and the decrease of the energy gap between the proton sd and fp shells, as well as the gap between the neutron $0f_{7/2-}$ and $0g_{9/2+}$ orbitals, when adding the two neutrons was emphasized. The identification of such $1p_{1h}$ -dominated levels is possible because of the low degree of collectivity in the Ni isotopes. This low collectivity results in comparably high excitation energies of their phonon excitations. Hence, the multiphonon excitations are found at comparably high excitation energies. As a consequence, in the Ni isotopes the strength carrying $1p_{1h}$ excitations can mix with only a limited number of surrounding states. Because the $1p_{1h}$ excitations are still dominant in the wave function of the observed states, their features (large ground-state branching ratios, comparably high $E1$ -excitation strength) are not totally obscured by a large number of admixtures of other microscopic structure. In more collective nuclei the $1p_{1h}$ excitations are embedded in an already considerable amount of $J^\pi = 1^-$ excitations of predominantly multiphonon or four-quasiparticle character. Mixing with these levels, which themselves do not carry any $E1$ strength, obscures the signatures of the $1p_{1h}$ excitations. Hence, in open-shell nuclei or heavier semimagic nuclei, the identification of the two-quasiparticle $1p_{1h}$ excitation is extremely difficult or simply impossible.

B. $M1$ -strength distribution for ^{60}Ni

The experimental $M1$ -strength distribution as obtained in the campaign performed in this work is presented in Fig. 8(b). It exhibits the typical pattern of a semimagic nucleus of several weaker excited levels at medium energies and two accumulations of $J^\pi = 1^+$ levels near 8 and 9 MeV excitation energy, respectively. The lower-lying levels can be associated with the $J = l + 1/2 \rightarrow J = l - 1/2$ spin-flip excitations. In the mass region under consideration these are the $1p_{3/2-} \rightarrow 1p_{1/2-}$ neutron, but even more important the $0f_{7/2-} \rightarrow 0f_{5/2-}$ excitations for either protons or neutrons. Via the residual dipole-dipole (spin-isospin) interaction these spin-flip excitations form an isoscalar mixture and an isovector mixture, which are known as the $M1$ resonances [40]. Indeed, the QPM confirms the proton and neutron $0f_{7/2-} \rightarrow 0f_{5/2-}$ $1p_{1h}$ excitations as dominant components in the $J^\pi = 1^+$ levels located in the mass region between 7 and 10 MeV. The experimentally observed fragmentation of the latter two resonances is caused by the interaction with multiphonon excitations coupling to $J^\pi = 1^+$.

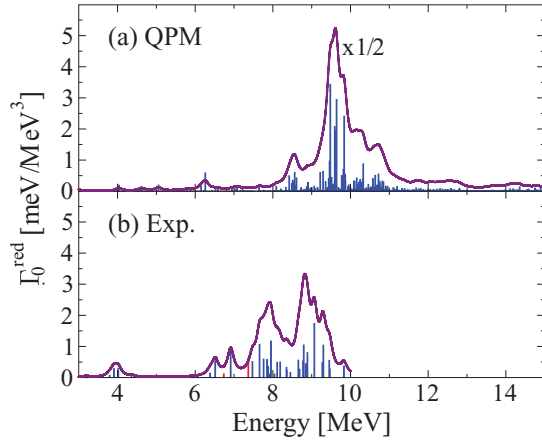


FIG. 8. (Color online) Distribution of $M1$ -excitation strength as obtained from QPM calculations (a) and the DHIPS measurements (b). Levels with a firmly assigned $J^\pi = 1^+$ are plotted as blue bars and $J = 1$ levels for which no parity information is known as red bars. Plotted is the reduced ground-state transition width, $\Gamma_0^{\text{red}} = \Gamma_0/E_\gamma^3$, as a function of the level excitation energy, E_R . The corresponding $B(M1, 0^+ \rightarrow 1^+)$ excitation strength calculates to $B(M1, 0^+ \rightarrow 1^+)[\mu_N^2] = 0.259\Gamma_0^{\text{red}}[\text{meV}/\text{MeV}^3]$. The solid line represents the sum of all levels' excitation strength folded with a Breit-Wigner curve of 200 keV width.

Obviously, as plotted in part (a) of Fig. 8 the QPM calculations overpredict the energy of the resonances and their total $B(M1)$ strength. In ^{60}Ni the total experimentally observed $B(M1) \uparrow$ strength is $\sum B(M1, 0^+ \rightarrow 1^+) = 4.1(3)\mu_N^2$. The total calculated $M1$ strength is $11.8\mu_N^2$. In the energy region up to 10 MeV the theoretical $M1$ strength is still $7.8\mu_N^2$. Applying the experimental sensitivity limit to the theoretical value, the latter sum strength shrinks to $6.3\mu_N^2$.

Concerning the branchings to lower-lying levels, the maximum experimental values, when the entire depopulation of the low-lying levels as seen in the $\text{HI}\bar{\gamma}\text{S}$ measurement ([50] and presented in Table VII) is attributed to the $J^\pi = 1^+$ levels, then the experimental and the total theoretical $M1$ strengths would agree well. However, the QPM calculations indicate that the $J^\pi = 1^+$ levels have only moderate branchings to lower-lying excited levels and their ground-state branching ratios are greater than 90% ($\Gamma_0/\Gamma \geq 0.9$). If this ratio is applied to the experimentally observed strength the theoretical strength is still $\approx 50\%$ too high. Hence, the deviation of the experimental and theoretical strengths indicates that the used quenching of the spin g factors, g_{eff}^S , with $g_{\text{eff}}^S = 0.8g_{\text{bare}}^S$ is not sufficient if all $M1$ strength is experimentally observed.

The experimentally observed $M1$ -strength distributions for ^{56}Fe [Fig. 9(a)] [38,39], ^{58}Ni [Fig. 9(b)] [38], and ^{60}Ni [Fig. 9(c)] are illustrated in Fig. 9. The folded $M1$ distributions of the two Ni isotopes exhibit a remarkable resemblance. The distribution of ^{56}Fe exhibits a slightly greater distance between the lower-lying isoscalar and the higher-lying isovector $M1$ resonance. Furthermore, in the Fe isotope near 3.5 MeV a stronger excited low-lying 1^+ state is observed. This level is associated with the $[2_1^+ \otimes 2_{ms}^+]_{1+}$ two-phonon level. The coupling of the first excited 2_1^+ level, associated with a symmetric coupling of proton and neutron excitations, and

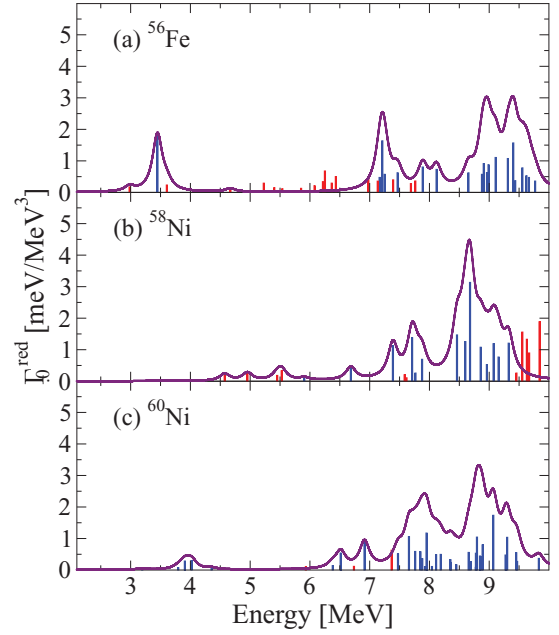


FIG. 9. (Color online) Distribution of $M1$ -excitation strength as measured for (a) ^{56}Fe [38,39], (b) ^{58}Ni [38], and (c) ^{60}Ni . Levels with a firmly assigned $J^\pi = 1^+$ are plotted as blue bars and $J = 1$ levels for which no parity information is known as red bars. Plotted is the reduced ground-state transition width, $\Gamma_0^{\text{red}} = \Gamma_0/E_\gamma^3$, as a function of the level excitation energy, E_R . The corresponding $B(M1, 0^+ \rightarrow 1^+)$ excitation strength calculates to $B(M1, 0^+ \rightarrow 1^+)[\mu_N^2] = 0.259\Gamma_0^{\text{red}}[\text{meV}/\text{MeV}^3]$. The solid line represents the sum of all levels' excitation strength folded with a Breit-Wigner curve of 200 keV width.

the 2_{ms}^+ mixed-symmetry state results in a quintuplet of levels with $J^\pi = 1^+ - 4^+$ [40,41]. Because the 2_{ms}^+ represents an out-of-phase motion of valence proton and valence neutron degrees of freedom, this kind of excitation is not present in semimagic nuclei. Consequently, no corresponding two-phonon $[2_1^+ \otimes 2_{ms}^+]_{1+}$ level can occur in the semimagic Ni isotopes. The $M1$ strength of this particular 1^+ level is of orbital character. Nevertheless, the interaction of these orbital $M1$ strengths with the spin-flip excitations via the residual spin-isospin/tensor interaction influences the energies of the latter. Furthermore, because protons in the $0f_{7/2-}$ subshell strongly interact attractively with neutrons in the $0f_{5/2-}$ subshell and repulsively with the neutrons in the $0f_{7/2-}$, an increase of relative energies of the latter two orbitals can be expected from the Fe to the Ni isotopes. Consequently, for ^{56}Fe the removal of the proton pair in the $0f_{7/2-}$ subshell increases the spin-orbit splitting of the two neutron f subshells. Therefore, the neutron $[0f_{5/2-}, 0f_{7/2-}]_{1+} 1p1h$ excitation is found at higher energy and the pattern of the $M1$ resonances changes.

In the energy region in which the $M1$ resonances are situated (6 to 10 MeV) the summed $M1$ strengths for the three isotopes are ^{56}Fe , $3.52(17)\mu_N^2$ [39]; ^{58}Ni , $3.77(10)\mu_N^2$; and ^{60}Ni , $3.94(27)\mu_N^2$. Here, only the firmly assigned 1^+ levels

were used to calculate the sum. The center of gravity, \bar{E} ,

$$\bar{E} = \frac{\sum_i E_i B(M1) \uparrow_i}{\sum_i B(M1) \uparrow_i}, \quad (9)$$

of the 1^+ levels in this energy region is calculated to be ^{56}Fe , 8.6 MeV; ^{58}Ni , 8.5 MeV; and ^{60}Ni , 8.1 MeV. The negligible change in excitation strength and average excitation energy indicates the collective nature of the observed $M1$ strength.

V. SUMMARY AND CONCLUSIONS

In the presented work a detailed picture of the photoresponse of ^{60}Ni was obtained. In total, 48 $J^\pi = 1^-$, 32 $J^\pi = 1^+$, 5 $J = 1$ levels with undetermined parity, and 7 $J^\pi = 2^+$ were observed. Additionally, the parity of 28 spin-1 levels in ^{58}Ni could be determined or, if it was previously known, confirmed.

The $E1$ -strength distribution exhibits a similar pattern as previously observed for ^{58}Ni [38] and ^{56}Fe [38,39]. All three isotopes exhibit a structure of stronger excited levels near 8 MeV excitation energy. In ^{60}Ni the branching behavior [50] identifies the levels forming this structure to have considerable $1p1h$ components in their wave functions. Furthermore, in ^{60}Ni this structure is found approximately 700 keV lower than in ^{58}Ni . The latter can be explained with a smaller gap between the neutron $0f_{7/2^-}$ and $0g_{9/2^+}$ subshells, resulting in a lower excitation energy for the corresponding $1p1h$ excitation. When

comparing similar energy regions the total $E1$ strength of the three isotopes is not subject to a significant change.

The $M1$ -strength distribution exhibits the expected pattern of some low-lying debris of $1p1h$ spin-flip excitations and the isoscalar and isovector $M1$ resonances near 8 and 9 MeV excitation energy. The comparison of the $M1$ -strength distributions of ^{58}Ni and ^{60}Ni reveals a remarkable resemblance. This is reflected in the total $B(M1) \uparrow$ strength determined for the $M1$ resonances in the two Ni isotopes, as well for ^{56}Fe . For all three isotopes a strength slightly less than $4\mu_N^2$ is observed. A comparison to QPM calculations reveals that the spin g factor needs, in addition to the already used quenching of $g_{\text{eff}}^S = 0.8g_{\text{bare}}^S$, an additional quenching.

ACKNOWLEDGMENTS

The authors are indebted to the staff of the H $\bar{\nu}$ GS facility and the S-DALINAC crew for the excellent photon beams. Furthermore, we thank U. Kneissl for valuable discussions and the access to the unpublished habilitation thesis of U. E. P. Berg. Financial support by the DFG under Grants No. SFB634, No. Pi393/2-1, No. SO907/1-2, and No. Zi 510/4-2 and U.S. DOE Grants No. DE-FG02-97ER41033, No. DE-FG02-97ER41042, and No. DE-FG02-97ER41041 is gratefully acknowledged. D. Savran acknowledges support by the Helmholtz Alliance Program of the Helmholtz Association (HA216/EMMI).

-
- [1] W. Greiner and J. A. Maruhn, *Nuclear Models* (Springer, Berlin, 1996).
- [2] M. N. Harakeh and A. van der Woude, *Giant Resonances* (Oxford University Press, Oxford, U.K. 2001).
- [3] R. M. Laszewski, *Phys. Rev. C* **34**, 1114 (1986).
- [4] R.-D. Herzberg *et al.*, *Phys. Lett. B* **390**, 49 (1997).
- [5] R.-D. Herzberg *et al.*, *Phys. Rev. C* **60**, 051307 (1999).
- [6] D. Savran, T. Aumann, and A. Zilges, *Prog. Part. Nucl. Phys.* **70**, 210 (2013).
- [7] J. Piekarewicz, *Phys. Rev. C* **83**, 034319 (2011).
- [8] P.-G. Reinhard and W. Nazarewicz, *Phys. Rev. C* **81**, 051303 (2010).
- [9] N. Paar *et al.*, *Rep. Prog. Phys.* **70**, 691 (2007).
- [10] V. G. Soloviev, *Theory of Atomic Nuclei, Quasiparticles and Phonons* (Institute of Physics, London, 1992).
- [11] K. Govaert *et al.*, *Phys. Rev. C* **57**, 2229 (1998).
- [12] D. Savran *et al.*, *Phys. Rev. Lett.* **100**, 232501 (2008).
- [13] D. Savran *et al.*, *Phys. Rev. C* **84**, 024326 (2011).
- [14] D. Savran *et al.*, *Phys. Rev. Lett.* **97**, 172502 (2006).
- [15] J. Endres *et al.*, *Phys. Rev. C* **80**, 034302 (2009).
- [16] J. Endres *et al.*, *Phys. Rev. Lett.* **105**, 212503 (2010).
- [17] J. Endres *et al.*, *Phys. Rev. C* **85**, 064331 (2012).
- [18] V. Derya *et al.*, *Nucl. Phys. A* **906**, 94 (2013).
- [19] W. Andrejtscheff *et al.*, *Phys. Lett. B* **506**, 239 (2001).
- [20] O. Wieland *et al.*, *Phys. Rev. Lett.* **102**, 092502 (2009).
- [21] P. Adrich *et al.*, *Phys. Rev. Lett.* **95**, 132501 (2005).
- [22] H. Fujita *et al.*, *Phys. Rev. C* **75**, 034310 (2007).
- [23] A. Tamii *et al.*, *Phys. Rev. Lett.* **107**, 062502 (2011).
- [24] I. Poltoratska *et al.*, *Phys. Rev. C* **85**, 041304 (2012).
- [25] C. Iwamoto *et al.*, *Phys. Rev. Lett.* **108**, 262501 (2012).
- [26] M. G. Guttormsen *et al.*, *Phys. Rev. Lett.* **109**, 162503 (2012).
- [27] M. Guttormsen, T. Ramsøy, and J. Rekestad, *Nucl. Instrum. Methods Phys. Res. A* **255**, 518 (1987).
- [28] A. Schiller *et al.*, *Nucl. Instrum. Methods Phys. Res. A* **447**, 498 (2000).
- [29] U. Kneissl, H. H. Pitz, and A. Zilges, *Prog. Part. Nucl. Phys.* **37**, 349 (1996).
- [30] U. Kneissl, N. Pietralla, and A. Zilges, *J. Phys. G* **32**, R217 (2006).
- [31] T. Hartmann, J. Enders, P. Mohr, K. Vogt, S. Volz, and A. Zilges, *Phys. Rev. C* **65**, 034301 (2002).
- [32] T. Hartmann, M. Babilon, S. Kamedzhiev, E. Litvinova, D. Savran, S. Volz, and A. Zilges, *Phys. Rev. Lett.* **93**, 192501 (2004).
- [33] J. Isaak *et al.*, *Phys. Rev. C* **83**, 034304 (2011).
- [34] G. Rusev *et al.*, *Phys. Rev. C* **79**, 061302 (2009).
- [35] S. Volz *et al.*, *Nucl. Phys. A* **779**, 1 (2006).
- [36] A. P. Tonchev *et al.*, *Phys. Rev. Lett.* **104**, 072501 (2010).
- [37] C. T. Angell *et al.*, *Phys. Rev. C* **86**, 051302(R) (2012).
- [38] F. Bauwens *et al.*, *Phys. Rev. C* **62**, 024302 (2000).
- [39] T. Shizuma *et al.*, *Phys. Rev. C* **87**, 024301 (2013).
- [40] K. Heyde, P. von Neumann Cosel, and A. Richter, *Rev. Mod. Phys.* **82**, 2365 (2010).
- [41] N. Pietralla, P. von Brentano, and A. F. Lisetskiy, *Prog. Part. Nucl. Phys.* **60**, 225 (2008).
- [42] G. Rusev *et al.*, *Phys. Rev. Lett.* **110**, 022503 (2013).
- [43] K. Sonnabend *et al.*, *Nucl. Instrum. Methods Phys. Res. A* **640**, 6 (2011).

- [44] <http://www.nndc.bnl.gov/ensdf/>
- [45] S. Agostinelli *et al.*, *Nucl. Instrum. Methods Phys. Res. A* **506**, 250 (2003).
- [46] H. J. Rose and D. M. Brink, *Rev. Mod. Phys.* **39**, 306 (1967).
- [47] G. Rusev, A. P. Tonchev, R. Schwengner, C. Sun, W. Tornow, and Y. K. Wu, *Phys. Rev. C* **79**, 047601 (2009).
- [48] H. R. Weller *et al.*, *Prog. Part. Nucl. Phys.* **62**, 257 (2009).
- [49] L. W. Fagg and S. S. Hanna, *Rev. Mod. Phys.* **31**, 711 (1959).
- [50] M. Scheck *et al.*, *Phys. Rev. C* **87**, 051304(R) (2013).
- [51] J. P. Schiffer *et al.*, *Phys. Rev. C* **87**, 034306 (2013).
- [52] U. E. P. Berg, habilitation thesis, Giessen University, 1985.
- [53] R. Moreh *et al.*, *Nucl. Phys. A* **224**, 86 (1974).
- [54] S. Raman, X. Ouyang, M. A. Islam, J. W. Starner, E. T. Journey, J. E. Lynn, and G. Martínez-Pinedo, *Phys. Rev. C* **70**, 044318 (2004).
- [55] V. Yu. Ponomarev *et al.*, *Nucl. Phys. A* **649**, 93 (1999).
- [56] A. Chakraborty *et al.*, *Phys. Rev. C* **83**, 034316 (2011).
- [57] W. Mettner *et al.*, *Nucl. Phys. A* **473**, 160 (1987).